A DNS study of the rheology of dense suspensions in plane Couette flow

Master Thesis

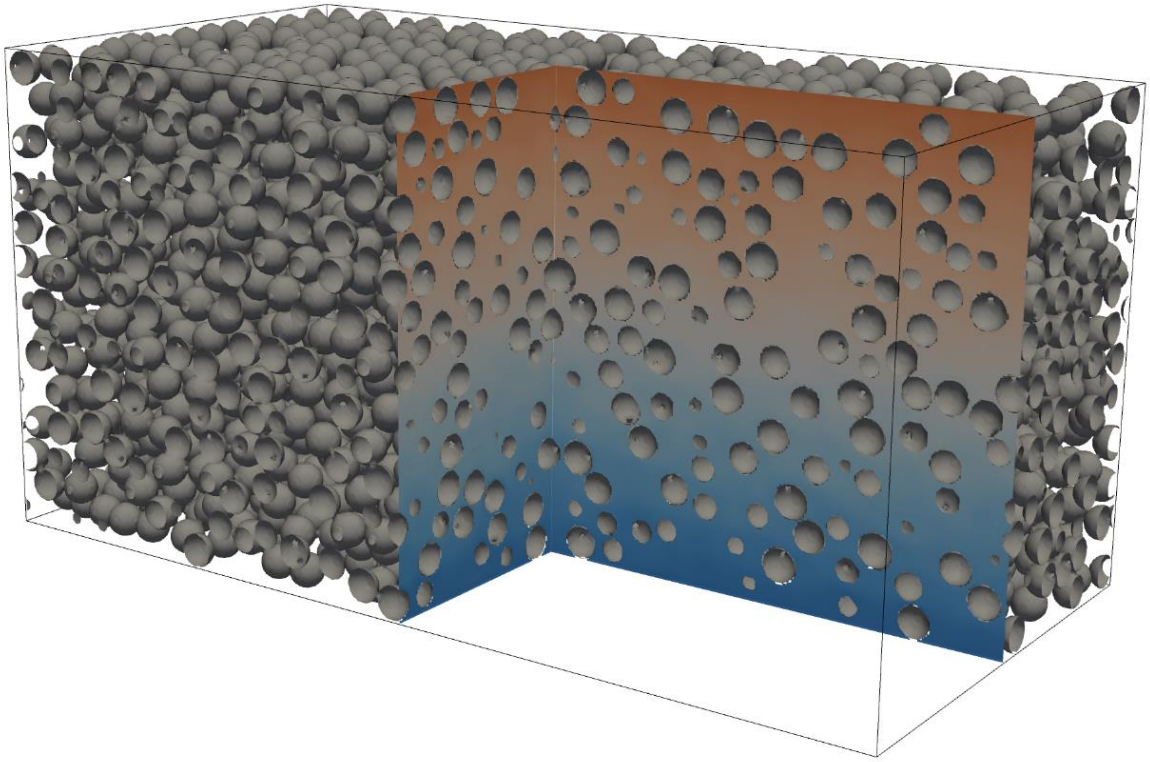

Fluid Mechanics - Process & Energy

June 16, 2022

Tim Nadorp

Thesis committee:

Dr. Ir. W.-P. Breugem (Daily supervisor)
Dr. D. Tam
Prof. Dr. A. van der Heijden
Dr. C. Chassange
Ir. W. Peerbooms (Supervisor)

Abstract

Dense suspensions can be found in various industrial and natural processes. A relatively new technique uses the principle of additive manufacturing to produce products from a wide variety of materials by printing with dense suspensions. To reach a high print quality the suspension rheology must be understood very well. Current knowledge about suspension rheology however lacks the capability of predicting the exact behaviour of a predefined suspension, especially for dense suspensions. Direct numerical simulation (DNS) in combination with a second order accurate immersed boundary method (IBM) (Breugem, 2012) can be a useful tool to research suspension rheology. However, currently no numerical results are known for suspensions close to the jamming limit produced with this method.

The current work validates the capability of the IBM to simulate dense suspensions by comparing produced results with existing numerical and experimental data. This is done by simulating a plane Couette flow for a range of particle volume fractions $\phi = 0.2 - 0.6$, all of which are simulated with two friction coefficients ($\mu_c = 0$ and 0.39). Furthermore, the focus is on Stokes flow of neutrally buoyant non-colloidal suspensions with monodisperse spherical particles and the channel height was chosen equal to 13.5 particle diameters. DNS has been used to analyse the suspension rheology in terms of mean concentration profiles, velocity profiles, interactions in the microstructure and particle stress profiles. Steady-state concentration profiles of the simulated cases show a particle layering effect close to the confining walls. This layering effect alters the suspension rheology significantly and for that reason the wall regions are analysed separately from the core region. For both regions the microstructure, the relative viscosity and the normal particle stresses are analysed. The results agree well with existing numerical results (Gallier et al., 2016) (Yeo & Maxey, 2010a). Comparison with experimental work (Dbouk et al., 2013) (Zarraga et al., 2000) shows that results for the relative viscosities of the unlayered core regions are lower in general, reasons for this difference can be higher friction factors or the use of non-spherical particles in experiments. However, the same asymptotic trend is observed for increasing ϕ. The maximum packing fraction ϕ_m was found by fitting the relative viscosities to the Marron & Pierce equation (Maron & Pierce, 1956), which gave $\phi_m = 0.69$ for $\mu_c = 0$ and $\phi_m = 0.635$ for $\mu_c = 0.39$. These results for ϕ_m are in good agreement with results from (Gallier et al., 2014).

In general the IBM turns out to be capable of reproducing existing numerical data. Furthermore, results have been obtained for suspensions closer to the jamming limit than known so far in numerical work on this particular flow regime. Besides that, the present results are obtained with an advanced soft-sphere collision model, including lubrication corrections for close approach of particles, which has been extensively validated with collision experiments in a previous study. Comparison of the results from this work with experimental data shows larger differences. The reason for this can be that the suspensions in experimental set-ups deviate from the idealized suspension in the simulations. Besides that experimental results differ significantly from each other, indicating that differences also exist between the experimental suspensions. These differences have to be clearly defined in order to make a valuable comparison. Therefore it is currently difficult to determine how accurately the IBM simulates suspension rheology.

Acknowledgements

This work could not have been made without the supervision of Wim-Paul Breugem and Wouter Peerbooms. I would like to thank both of them for all the in-depth conversations we had about simulating dense suspensions. The numerical routine developed by Wim-Paul was essential for this work and to me the capabilities of his software are truly astonishing. Besides that, his excellent knowledge on multiphase flows led to various key insights during this project. In addition, my appreciation goes to Wouter Peerbooms for sharing his literary knowledge on the topic and his experience with postprocessing of numerical data. I want to thank Antoine van der Heijden for providing insight into the practical problems that arise during 3D-printing with dense suspensions, which is the motivation for this work. Last but not least I would like to thank the members of the graduation committee: D. Tam and C. Chassange.

Contents

1 Introduction 6
2 Literature study 8
2.1 Dimensional analysis 8
2.2 Suspension rheology 10
2.3 Suspension flow in confinement 18
2.4 Numerical methods 20
2.5 Discussion 23
3 Problem statement and objectives 23
4 Method 24
4.1 Governing equations 24
4.2 Numerical method 25
4.3 Contact model 26
4.4 Lubrication correction 27
5 Simulations 28
5.1 Initial particle positions 29
5.2 Convergence 30
6 Postprocessing 32
6.1 Superficial averages 32
6.2 Pair distribution function 32
6.3 Particle stress tensor 33
7 Results 36
7.1 Stress budgets 37
7.2 The effect of confinement 38
7.3 Microstructure 40
7.4 Viscosity 44
7.5 Normal particle stresses 48
7.6 The effect of the coefficients of restitution 52
8 Conclusion and recommendations 53
8.1 Recommendations 54
Bibliography 55

1 Introduction

Suspensions can be found in a wide variety of practical applications, many of which are industrial. Examples are the transportation of food, cosmetics, and fresh concrete through pipelines (Figure 1-1a). The rheology of the simplest imaginable suspensions of a neutrally buoyant non-colloidal suspension of hard spheres in Stokes flow already shows very complex behaviour, especially for high particle volume fractions. Typical observed phenomena are jamming, shear thinning, shear thickening and normal stress differences. Precise knowledge of when and how these phenomena occur can help optimizing processes and reducing energy consumption in industry. Besides that also natural processes involve suspension flows, for example blood flow (Figure 1-1b), submarine avalanches and sediment transport in rivers (Figure 1-1c). Therefore, a better insight in suspension rheology will also help understanding and predicting natural phenomena.

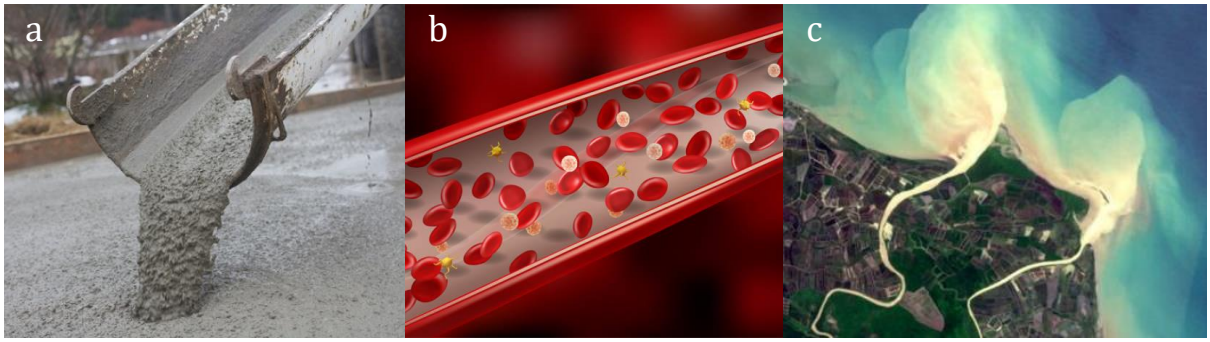

Figure 1-1, Examples of suspension flows. a: concrete flow (Southeast Asia Construction, 2018), b: blood flow (Vecteezy, 2022), c: sediment transport in rivers (Stone-Ideas, 2020)

A relatively new application of suspensions can be found in additive manufacturing. FDM (Fused Deposition Modelling) 3D-printers normally make use of a solid plastic filament wire that is melted to construct a print layer by layer. The applicability of this technique can be enlarged by making use of suspensions instead of filament wire. Printing with suspensions makes it possible to produce prints from materials like concrete (Figure 1-2a), paper pulp (Figure 1-2b), edible materials (Figure 1-2c), ceramics (Schwentenwein & Homa, 2014) and even organic materials (McCormack et al., 2020). Note that printable suspensions are generally relatively dense suspensions such that high quality products can be produced. In this literature study we define dense suspensions as suspensions with a particle volume fraction $\gg 1\%$ up until the jamming limit. The viscosity of suspensions increases rapidly with the particle volume fraction, making transportation of dense suspensions difficult. In the worst case the jamming limit is reached such that the suspension will not flow at all. Besides that also particle segregation resulting in non-uniform spatial particle distributions threatens the print quality (Bae & Halloran, 2019). Research with respect to rheological behaviour of suspensions will therefore contribute to the development of this technique and the improvement of print quality of printed products.

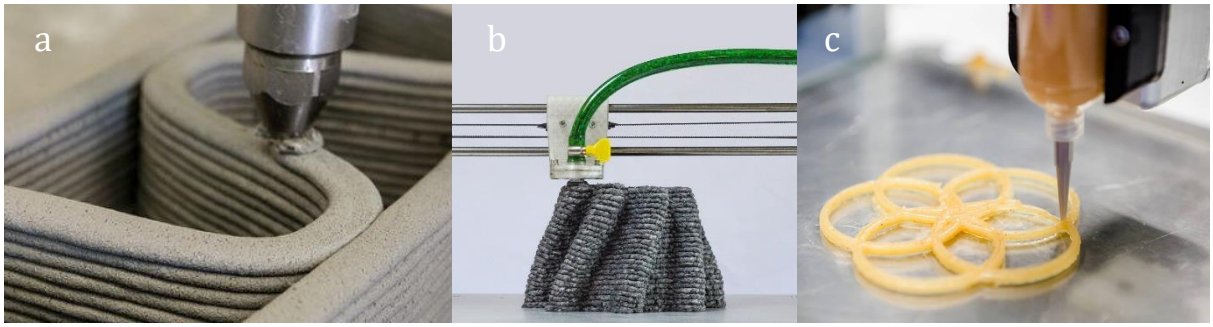

Figure 1-2, Examples of 3D printed suspensions. a: concrete (Material District, 2020), b: paper pulp (Beer Holthuis, 2018), c: edible material (3DPRINTING.com, 2019)

The rheology of suspensions has been a topic of research since the beginning of the 20th century. Nonetheless the mechanisms behind the rheological properties are still far from understood. From an engineering point of view this is problematic since it is not possible to exactly predict pressure drop or the occurrence of the jamming condition. Suspension flows in the viscous regime are the most researched but even in that regime big open questions remain, for example the mechanism behind non-Newtonian behaviour in viscosity dominated suspension flow. Inertial suspension flows are less researched, but direct numerical simulations can be of large value for this in the future. In this study the main focus is on a plane Couette flow driven by two walls moving at the same but opposite velocity. Apart from particle layering effects close to the walls the shear rate will be equal throughout the domain such that shear-induced particle migration (typically observed in Poiseuille flow) will not play a role. Therefore the solid distribution will be homogeneous, which is convenient for statistical analysis of the rheological flow behaviour.

This work starts with a literature study in order to sort out the current state of knowledge related to suspension rheology and suspension simulation techniques. After that a detailed explanation is given about the numerical method used in this study. Section 5 gives details about the simulated domain and, the boundary conditions and the parameter space is defined. Various postprocessing routines are explained in section 6, which are used to produce the results that are finally presented in section 7.

2 Literature study

Suspensions are considered a class of complex fluids that consist of particles suspended in a liquid. This class can be differentiated in subclasses according to the physical nature of the suspended particles. In this work we are mainly interested in non-colloidal dense suspensions of hard spheres in Stokes flow with very low Galileo numbers. Suspensions can be considered non-colloidal when the particle diameter is larger than approximately 10 micron such that Brownian forces can be neglected. For suspensions with low Galileo numbers the viscous forces dominate the gravitational forces such that settling can be neglected. However, for suspensions in the Stokes regime inertial forces are not relevant, so suspensions with low Galileo numbers are effectively the same as neutrally buoyant suspensions.

In this section scientific literature is addressed in order to sort out the current state of knowledge related to the rheology of suspensions with the characteristics mentioned above. The study is based on scientific articles that are of interest for this topic and all relevant aspects are covered in this section. First a dimensional analysis gives clarity about the assumptions we make and the role of the different variables. Then the rheological behaviour of suspensions is discussed by explaining the effects of shear stress on a suspension and their origins if known. After that the behaviour of dense suspensions in plane Couette flow and the effect of confinement are described. And finally different numerical methods capable of simulating suspension flow are given.

2.1 Dimensional analysis

The viscosity of a suspension of hard spheres in a Newtonian fluid in Couette flow can be described as a function of the following parameters (Stickel & Powell, 2005):

$$\eta_s = f\left(d, \rho_s, n, \eta_f, \rho_f, kT, \dot{\gamma}, t\right), \tag{2.1}$$

where d is the particle diameter (for a monodisperse suspension), ρ_s is the particle density, n is the number concentration, η_f is the fluid viscosity, ρ_f is the fluid density, kT is the thermal energy (with k the Boltzmann constant), $\dot{\gamma}$ is the rate of shear and t is the time. After a dimensional analysis the following dimensionless groups can be formed:

$$\eta_r = \frac{\eta_s}{\eta_f}, \qquad \phi = \frac{4\pi}{3} n \left(\frac{d}{2}\right)^3, \qquad \rho_r = \frac{\rho_s}{\rho_f}, \qquad Pe_{\dot{\gamma}} = \frac{6\pi\eta_f d^3 \dot{\gamma}}{kT}, \qquad Re_{\dot{\gamma}} = \frac{\rho_f d^2 \dot{\gamma}}{\eta_f}, \qquad t_r = \frac{tkT}{\eta_f d^3},$$

$$\eta_r = f\left(\phi, \rho_r, Pe_{\dot{\gamma}}, Re_{\dot{\gamma}}, t_r\right), \tag{2.2}$$

where η_r is the relative dimensionless viscosity relating the suspension viscosity to the fluid viscosity. Different flow regimes can be defined by using the dimensionless numbers above. In the case of a neutrally buoyant ($\rho_r = 1$) steady-state flow ($t_r \gg 1$) the relative viscosity will only be a function of ϕ, $Re_{\dot{\gamma}}$ and $Pe_{\dot{\gamma}}$. For a certain volume fraction the shear rate dependence can then be mapped in a $Pe_{\dot{\gamma}} Re_{\dot{\gamma}}$ – plane as shown in Figure 2-1. For small $Pe_{\dot{\gamma}}$ Brownian forces dominate viscous forces causing shear thinning behaviour and for large $Re_{\dot{\gamma}}$ inertial forces dominate viscous forces causing shear thickening behaviour (Stickel & Powell, 2005).

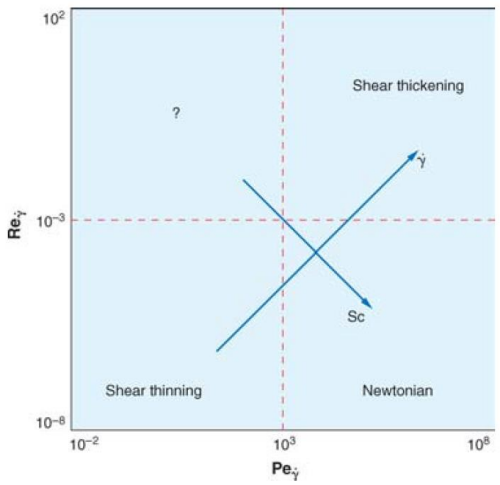

Figure 2-1, Flow regime map based on a dimensional analysis (Stickel & Powell, 2005).

In the special case of a non-colloidal ($Pe_{\dot{\gamma}} \to \infty$) flow in the Stokes regime ($Re_{\dot{\gamma}} \ll 1$) Brownian forces and inertial forces are negligible such that there is only the viscous force scale. Therefore the suspension rheology is expected be independent of the shear rate and the dependency of η_r reduces to:

$$\eta_r = f(\phi) \tag{2.3}$$

This means that for this special case the suspension viscosity is only a function of the particle volume fraction. The independence of the relative viscosity with respect to the shear rate can be referred to as Newtonian behaviour. Note however that other non-Newtonian effects like normal stress differences will still be present in this regime. These effects are further explained in section 2.2.2.

Suspension flow of higher $Re_{\dot{\gamma}}$ is less researched, but more complex behaviour can be expected since inertial forces will compete with viscous forces. Various instabilities can arise depending on the flow type (Morris, 2020). Suspension flow of lower $Pe_{\dot{\gamma}}$ are referred to as colloidal suspensions. In this regime the particles are small enough to experience Brownian motion, this will result in more uniformly distributed particles in general (Morris, 2009).

For suspensions with $\phi \gtrsim 0.4$ interparticle forces will dominate the viscous forces (Guazelli & Pouliquen, 2018). Interparticle forces have a normal and a tangential part which are related to each other by:

$$\boldsymbol{F}_{p,tangential} \leq \mu_c \boldsymbol{F}_{p,normal}, \tag{2.4}$$

where μ_c is the Coulomb coefficient of sliding friction. One could argue that the relative viscosity of a non-colloidal neutrally buoyant suspension in Stokes flow will also depend on this friction coefficient (Morris et al., 2018).

2.2 Suspension rheology

Suspension rheology is usually described for the general case of a suspension sheared in Couette flow. The advantage of the description based on a Couette flow is that the suspension experiences an approximately constant shear stress over the complete volume, given by:

$$\tau = \eta_s \dot{\gamma}, \tag{2.5}$$

where the shear rate is defined as $\dot{\gamma} = U/h$, with U the velocity difference between the upper and the lower plate and h the gap width. Various types of Couette flow rheometers are used to determine suspension viscosity making use of this relation. This flow geometry is assumed in this section unless stated otherwise.

2.2.1 Viscosity

The viscosity of monodisperse, neutrally buoyant, non-colloidal suspensions of hard spheres in Stokes flow can be described as a function of the particle volume fraction as shown before. The suspension viscosity can therefore be defined as:

$$\eta_s = \eta_f \eta_r(\phi). \tag{2.6}$$

The dependency on the particle volume fraction has been a field of research since the early 1900s with the first significant result by (Einstein, 1911). He found a relation for the viscosity of non-Brownian suspensions in the dilute limit $\phi \to 0$ by considering perturbations in the fluid phase caused by a single solid particle in shear flow. Shear flows can be decomposed in a rotating motion and a straining motion as visualised in Figure 2-2. Hard spheres tend to co-rotate with the surrounding fluid, but will resist against straining. The straining motion creates a stresslet acting on the particle, which increases the viscous dissipation rate and hence the effective viscosity of the suspension. Einstein found the following relation:

$$\eta_r = 1 + \frac{5}{2}\phi. \tag{2.7}$$

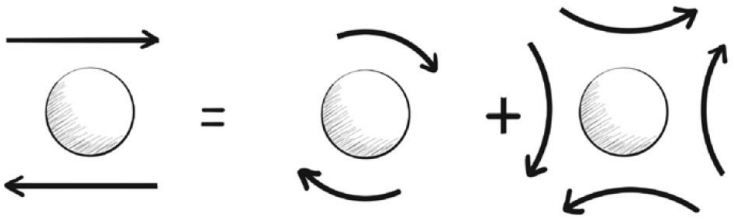

Figure 2-2, The decomposition of a shearing motion into a rotating motion and a straining motion (Guazelli & Pouliquen, 2018).

For larger volume fractions particle interactions will play a significant role. Particles will find themselves in the disturbance flow of other particles as the distances between particles get smaller. Later the relation from Einstein was improved, by taking particle interactions in the semi-dilute regime ($\phi \approx 0.10 - 0.15$) into accounting. This resulted in the following relation (Batchelor & Green, 1972):

$$\eta_r = 1 + \frac{5}{2}\phi + 6.95\phi^2. \tag{2.8}$$

Deriving the particle volume fraction dependence for the more dense regime is too complex to achieve in an analytical manner, mainly due to the amount of multibody interactions for increasing volume fractions. Furthermore, the rheology will not only be influenced by hydrodynamic interactions but also by direct mechanical contact between particles. For large particle volume fractions the mechanical contact interactions will dominate the flow behaviour (Guazelli &

Pouliquen, 2018). In this regime the suspension viscosity will eventually go to infinity when the jamming transition is reached ($\phi = \phi_m$); in this state the particle volume fraction is so high that the suspension no longer behaves like a fluid when sheared in Couette flow. Various experiments are performed in this regime using different kinds of rheometers. The exact numerical value of ϕ_m differs between experiments, but after normalisation the results all follow the same trendline. One of the most famous correlations, making use of this normalisation is the Krieger-Dougherty correlation (Krieger & Dougherty, 1959):

$$\eta_r = \left(1 - \frac{\phi}{\phi_m}\right)^{-\lambda}, \tag{2.9}$$

where $\lambda = 2$ gives the best representation and the relation is called the Maron-Pierce equation in that case (Maron & Pierce, 1956). Another famous correlation is Eilers' correlation (Eilers, 1941), which gives reasonable values for the complete range of particle volume fractions:

$$\eta_r = \left(1 + \frac{\frac{5\phi}{4}}{1 - \frac{\phi}{\phi_m}}\right)^2. \tag{2.10}$$

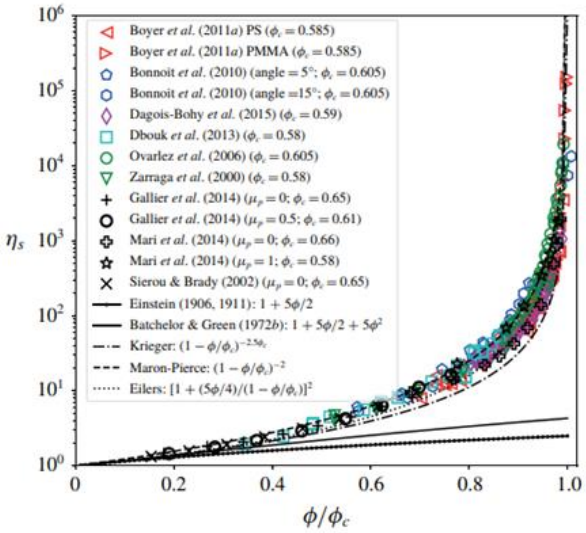

Figure 2-3, The suspension viscosity as a function of the normalised particle volume fraction for numerical and experimental results and correlations (Guazelli & Pouliquen, 2018).

The various correlations along with a number of experimental results are plotted in Figure 2-3. From this figure it is clear that the suspension viscosity increases with an increasing particle volume fraction. In the dilute regime this increase in viscosity is caused by the distortion of the shear flow and for slightly denser suspensions particle interactions of three or more particles will also increase the viscosity (Stickel & Powell, 2005). In this dilute regime particles will likely not make any contact since a lubrication film prevents this, and in theory lubrication forces will make contact between smooth particles impossible. However, at higher volume fractions the distance between particles will be smaller, in fact so small that the distance between two particles can be of the same order as the roughness of the particles itself. Therefore mechanical contact between particles will occur, which means that the particle friction factor μ_c will be relevant for dense suspensions. At a certain particle volume fraction ϕ_m the jamming condition will be reached. The viscosity of the suspension will go to infinity at the jamming condition meaning that from this point it's not possible anymore to flow the suspension. This condition is also referred to as the maximum flowable volume fraction. The fraction at which this happens is dependent on

polydispersity (Pednekar et al., 2018) and the interparticle friction coefficient (Gallier et al., 2014). The maximum flowable volume fraction is in general smaller than the random close packing fraction ϕ_{RCP}, which is the volume fraction that can be reached by vibrating or continuously tapping granular suspensions (for monodisperse spherical particles: $\phi_{RCP} \approx 0.64$) (Guazelli & Pouliquen, 2018). As a result of the solid-like behaviour at the jamming condition the suspension will exhibit a yield stress.

2.2.2 Normal particle stress

The change in viscosity does not give a complete view of the rheology of a suspension. Normal stresses are also affected by the particles present in the fluid. To take this into account the determination of the mixture model stress tensor for suspensions requires the term $\boldsymbol{\sigma_p}$ for the particle pressure (Stickel & Powell, 2005). The complete stress tensor is given by:

$$\boldsymbol{\sigma} = -p_f \boldsymbol{I} + 2\eta_f \boldsymbol{e} + \boldsymbol{\sigma}_p, \tag{2.11}$$

where p_f is the suspending fluid pressure and $\boldsymbol{e}$ is the rate-of-strain tensor. The particle pressure is a result of interparticle collisions in the sheared suspension. Particles will impose a positive pressure on the bounding walls, the fluid however will compensate for this pressure since it is incompressible resulting in a negative normal stress. Normal stress is present in all three normal directions. Just like the shear stress, these normal stresses scale viscously. The normal particle stresses can be described by:

$$\boldsymbol{\sigma_p^{normal}} = -\eta_f |\boldsymbol{e}| \begin{pmatrix} \eta_{n,x}(\phi) & 0 & 0 \\ 0 & \eta_{n,y}(\phi) & 0 \\ 0 & 0 & \eta_{n,z}(\phi) \end{pmatrix}, \tag{2.12}$$

where $|\boldsymbol{e}|$ is equal to the rate of strain $\dot{\gamma}$. The functions $\eta_{n,i}(\phi)$ all tend to 0 in dilute regime and just like the viscosity converge while approaching the jamming condition (Guazelli & Pouliquen, 2018). Directions x, y and z represent the vorticity, the velocity and the velocity gradient directions respectively as indicated in Figure 2-4.

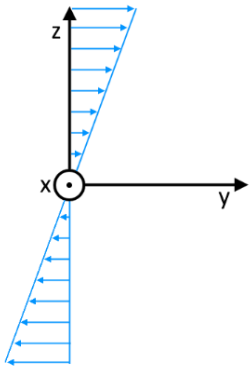

Figure 2-4, Axis orientation for shear flow

For single-phase fluid flow all normal stresses will be equal at a certain location in the fluid. But unlike single-phase flows, suspension flows can show normal stress differences. The first and second normal-stress differences are defined as:

$$N_1 = \sigma_{p,yy} - \sigma_{p,zz}, \tag{2.13}$$

$$N_2 = \sigma_{p,zz} - \sigma_{p,xx}. \tag{2.14}$$

Normal stress differences in sheared suspensions are caused by nonuniform relative particle distributions. The particles in a suspension will be more likely to find themselves in certain

regions with respect to each other compared to other regions. This will be explained in more detail in section 2.2.4. Using equation (2.12) the particle pressure tensor the normal-stress differences can be rewritten as the shear stress times a function of the volume fraction:

$$N_1 = \alpha_1(\phi)|\tau|, \tag{2.15}$$

$$N_2 = \alpha_2(\phi)|\tau|. \tag{2.16}$$

Experimental and numerical data sets of $\alpha_1(\phi)$ and $\alpha_2(\phi)$ are given in Figure 2-5. The sign of $\alpha_1(\phi)$ varies for the different data sets, an explanation of these variations can be the occurrence of particle layering near the wall (which promotes a positive sign) (Guazelli & Pouliquen, 2018). The sign of $\alpha_2(\phi)$ is accepted to be negative and in general $|N_1| < |N_2|$ (Stickel & Powell, 2005). The normal stress differences are caused by both hydrodynamic and particle contact forces, but the contributions are not equal. Numerical work of (Gallier et al., 2014) shows that N_1 is mostly of hydrodynamic origin while N_2 is mostly caused by contact forces, the contributions to the stress differences for varying volume fraction are given in Figure 2-6. The difference in particle contribution can be explained by the fact that particle collisions will occur more or less equally in the velocity and the velocity gradient direction, but significantly less in the vorticity direction: $\sigma_{p,xx} \ll \sigma_{p,yy} \approx \sigma_{p,zz}$ (Gallier et al., 2014).

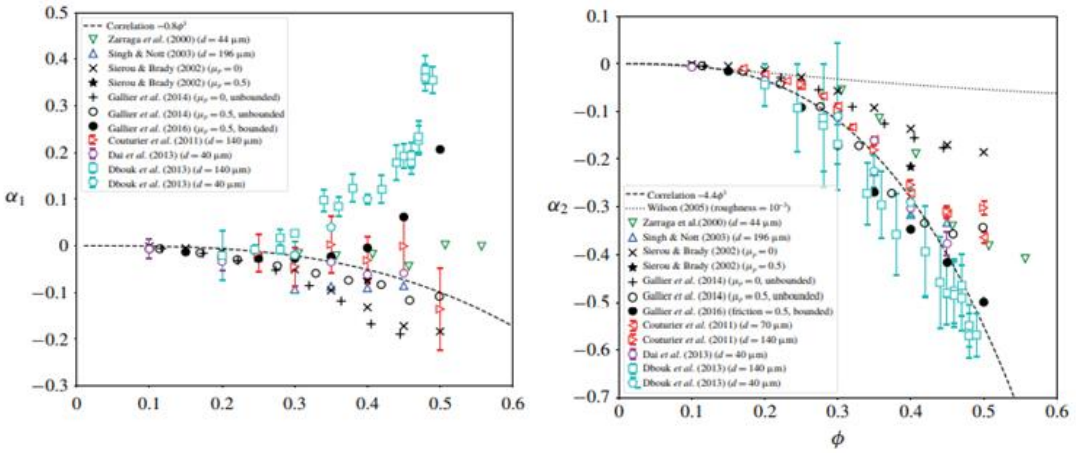

Figure 2-5, Normal-stress difference coefficients α_1 (left) and α_2 (right) as a function of ϕ for multiple experimental and numerical results (Guazelli & Pouliquen, 2018).

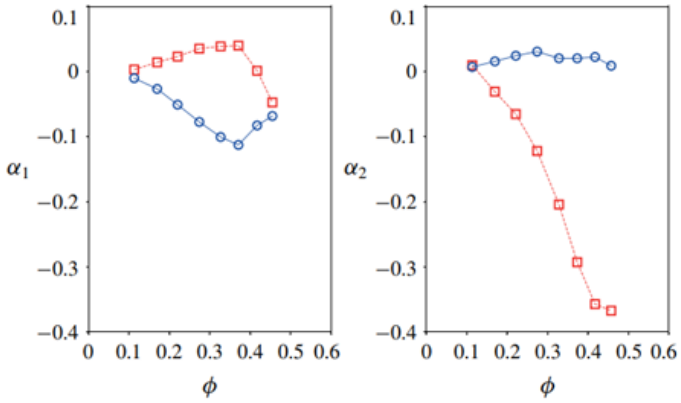

Figure 2-6, Hydrodynamic and contact contributions of the normal stress differences. Red squares and blue circles represent contact and hydrodynamic forces respectively (Guazelli & Pouliquen, 2018).

The total isotropic pressure in the suspension will be equal to $p = p_f + p_p$, with $p_p = -\frac{1}{3} tr(\boldsymbol{\sigma_p})$ (Stickel & Powell, 2005). The particles in a dense suspension sheared between two

parallel plates will exert a positive pressure p_p onto the plates. But this pressure will be compensated by a negative pressure in the fluid phase, since the suspension is incompressible. So the particles will push on the wall, and the wall will pull on the fluid (Guazelli & Pouliquen, 2018). This particle pressure can be considered analogue to an osmotic pressure.

2.2.3 Friction factor dependence

In the dimensional analysis it was already mentioned that besides the particle volume fraction also the interparticle friction factor can be of interest for predicting the rheological properties of a suspension. The friction factor is defined as the ratio of the tangential and the normal contact forces:

$$\mu_c = \frac{\boldsymbol{F}_{c,tangential}}{\boldsymbol{F}_{c,normal}} \tag{2.17}$$

Besides that it also defines a limit for the tangential forces given by: $\boldsymbol{F}_{p,tangential} \leq \mu_c \boldsymbol{F}_{p,normal}$. Tangential forces that tend to exceed this limit will cause slip between the two surfaces. The effect of the friction factor on rheological properties is hard to determine experimentally since it is difficult to vary the friction factor itself. In numerical simulations however the value can be changed very easily. Simulations of (Gallier et al., 2014) predict the relative viscosity for different friction factors. These results were later compared to experimental results, as shown in Figure 2-7. From this it becomes clear that simulations with higher friction factors agree better with the experimental results. We can also conclude that the hydrodynamic contribution of the relative viscosity is not affected by the increase in friction factor, the increase in viscosity originates from the contact contribution only. The friction factor also influences the maximum flowable volume fraction ϕ_m at which jamming will occur, higher friction factors will lead to lower ϕ_m (Guazelli & Pouliquen, 2018). This effect is also visible in Figure 2-7 as the viscosity for suspensions with higher friction factors diverge at lower volume fractions.

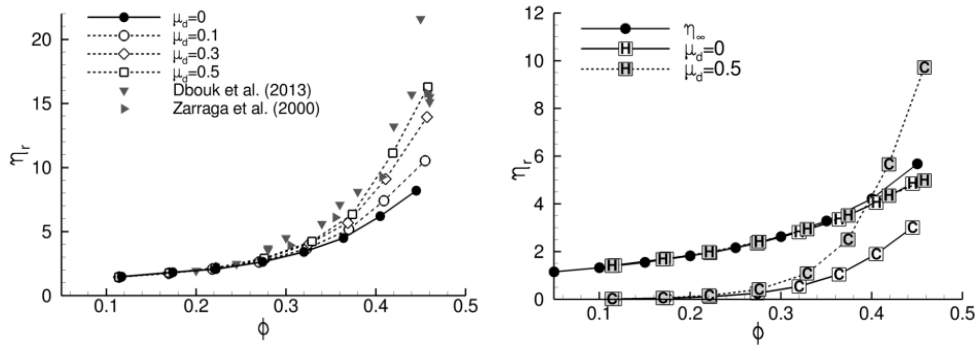

Figure 2-7, Left: relative viscosity for varying friction factor, Right: Hydrodynamic and contact contributions for two friction factors (Gallier et al., 2014).

The first and second normal stress differences also show a friction factor dependence, as shown in Figure 2-8. Decomposing the stress differences in hydrodynamic and contact contributions shows that contact forces are mainly responsible for this friction factor dependence. The first normal stress difference N_1 becomes less negative for increasing friction factor while N_2 becomes more negative, besides that the effect on N_2 is significantly larger. This can be explained by the fact that N_2 is for the largest part caused by contact interactions while N_1 has a hydrodynamic origin.

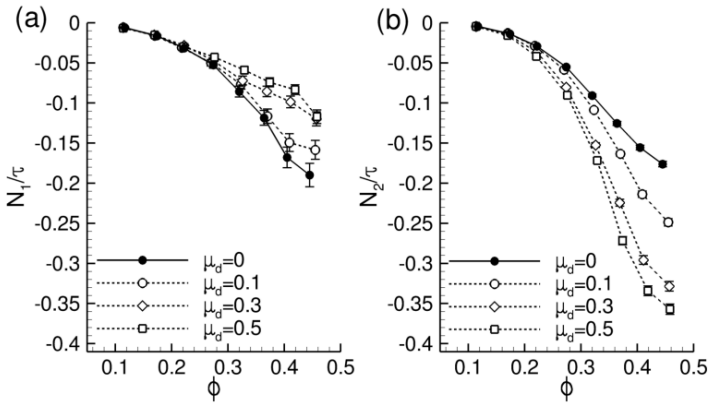

Figure 2-8, Friction factor dependence of the first and second normal stress differences (Gallier et al., 2014).

2.2.4 Microstructure

The rheology of a suspension is completely determined by interactions on the microscale. In Stokes flow the Navier-Stokes equations become linear which implies that the flow is reversible. The trajectories of particle interactions between only two particles will therefore be mirror symmetric across the $y = 0$ plane (Morris, 2009), this is illustrated in Figure 2-9. This means that the likelihood of finding another particle on the point of symmetry across this plane is equal for every point outside the particle. This pure hydrodynamic interaction therefore predicts Newtonian behaviour without any shear rate dependence. However non-Newtonian behaviour is typically observed in experimental research, which is an effect of irreversibility in the particle interactions. These irreversibilities arise from two mechanisms (Morris, 2009), the first of which is because of the chaotic behaviour of multibody interactions. For dense suspensions particle interactions will likely occur between more than two particles which introduces nonlinearity in the hydrodynamic resistance. The second mechanism is due to particle distances getting infinitesimally small due to lubrication forces, distances even decrease to the same order of the particle roughness. At that point it's reasonable to assume that interparticle contact forces are present.

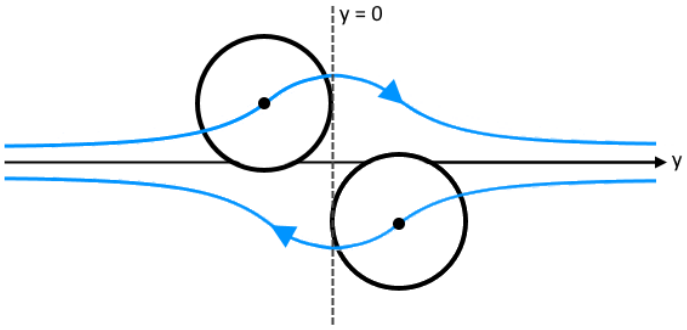

Figure 2-9, Particle path-lines of two particles in Couette flow

A much used tool for representing the microstructure of a suspension is the pair distribution function (PDF) $g(\boldsymbol{r})$. This function gives the probability of finding another particle at distance $\boldsymbol{r}$ from a particle. It is usually normalised with the probability of finding another particle in a perfectly homogeneous particle distribution, such that the $g(\boldsymbol{r}) \approx 1$ far away from the origin. The PDF is in general hard to determine for experiments, however experimental PDF's have been produced using an index-matching technique (Blanc et al., 2013). Results are given in Figure 2-10. For a dilute suspension with $\phi = 0.05$ the PDF shows a slight asymmetry in the distribution across the $y = 0$ plane. This asymmetry can be explained by the particle roughness playing a role when

particles get close to each other, as mentioned before. For larger particle volume fractions we can see that the high pair correlation zone rotates to the compressional quadrant ($yz < 0$). At even higher ϕ this zone splits into two zones with one roughly at the top/bottom and the other one on the velocity direction of the particle. For $\phi = 0.55$ the jamming condition is almost reached, there we can see that a layered structure exists. The rotation of the high pair correlation zone towards the velocity direction agrees with the change in sign for the contact contribution of N_1 proposed by (Gallier et al., 2014). Direct numerical simulation suggests that contact forces promote a positive N_1 in the dilute regime as contact occurs mainly in the velocity gradient direction. For larger particle volume fractions a negative N_1 is promoted by the high pair correlation zones shifting to the velocity direction.

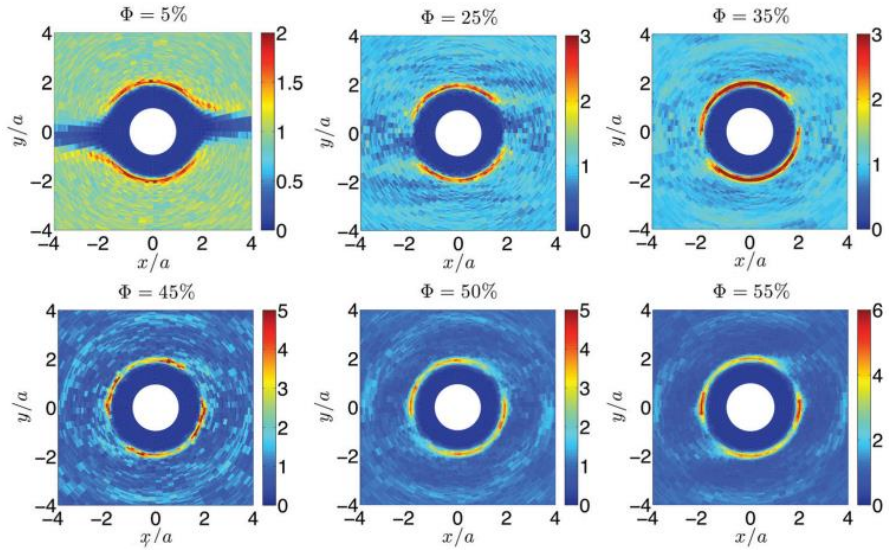

Figure 2-10, Experimental PDF for different particle volume fractions in the sheared plane (Blanc et al., 2013). Note: the sheared plane here is defined as the xy-plane in contrast to the standard in this work.

2.2.5 Pressure imposed rheology

The rheology of a suspension can also be described from the perspective of granular flows immersed in a fluid. Examples of such flows are submarine avalanches in geophysics or flow of heavy grains in a tumbler. This approach originates from studies on dry granular flows. The volume fraction is typically not constant for such flows, instead the pressure on the granular bed is fixed. When the pressure P^p is prescribed dry granular flows are determined by only one dimensionless number, the Inertial number:

$$I = d\dot{\gamma}\sqrt{\rho_p/P^p} = \frac{t_{inertial}}{t_{strain}}, \tag{2.18}$$

where $t_{inertial} = d\sqrt{\rho_p/P^p}$ is the inertial time scale pertaining to the microstructure and $t_{strain} = 1/\dot{\gamma}$ is the time of strain pertaining to the macrostructure. A similar expression can be formulated for suspensions in Stokes flow, here the flow is determined by the Viscous number:

$$I_v = \frac{\eta_f \dot{\gamma}}{P^p} = \frac{t_{viscous}}{t_{strain}}, \tag{2.19}$$

where $t_{viscous} = \eta_f/P^p$ is the viscous timescale. Note that in this work we assume that $t_{viscous} \ll t_{inertial}$ and hence the viscous timescale is more important. For suspensions two constitutive laws can be expressed as function of I_v:

$$\tau = \mu(I_v)P^p, \tag{2.20}$$

$$\phi = \phi(I_v), \tag{2.21}$$

where μ is the effective friction coefficient. The particle volume fraction is a function of the Viscous number since fluid can enter and leave the suspension. In order to plot these two relations experiments have been performed using rheometers with one porous side (Boyer et al., 2011). This allows the fluid to pass but it keeps the particles in the measured domain such that the particle volume fraction is not fixed. The pressure on the bed was fixed for the experiments. Results of these experiments are given in Figure 2-11. It is clear that τ is an increasing function of $\dot{\gamma}$, which is why μ is an increasing function of the Viscous number. For very small Viscous numbers there still remains an effective friction factor of approximately 0.32, this value is similar to friction factors for dry-granular flows. The particle volume fraction is a decreasing function of the Viscous number, which can be explained by the increasing particle pressure for larger strain rates. For very small Viscous numbers the maximum volume fraction is reached in the bed.

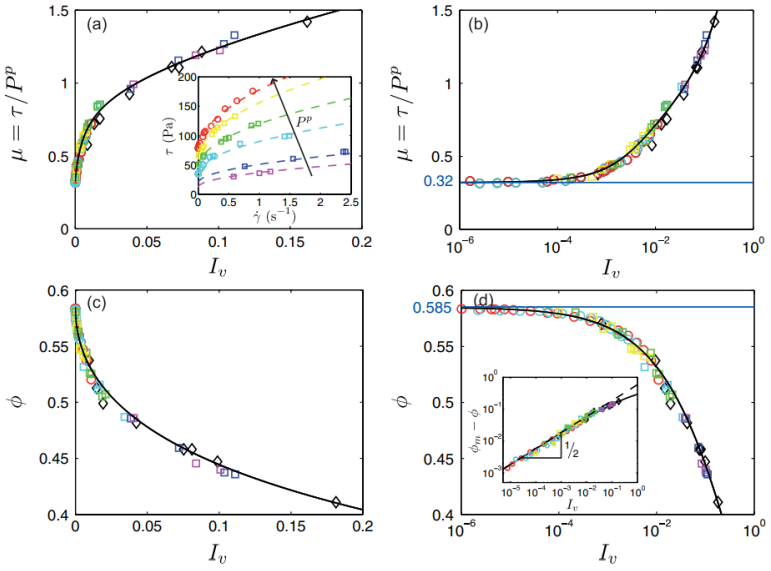

Figure 2-11, The effective friction coefficient and particle volume fraction versus the Viscous number I_v (Boyer et al., 2011).

This pressure imposed description can be related to the case of a constant volume by defining the relative viscosity and the normal stress to the Viscous number:

$$\eta_r(\phi) = \frac{\mu[I_v(\phi)]}{I_v(\phi)}, \tag{2.22}$$

$$\eta_{n,z}(\phi) = \frac{1}{I_v(\phi)} \tag{2.23}$$

Conversion from Viscous number dependence to volume fraction dependence of the experimental data from (Boyer et al., 2011) agrees well with Eilers' fit and the Krieger-Dougherty correlation.

2.3 Suspension flow in confinement

The rheology of suspensions is usually experimentally determined with rheometers in confined domains, for example a plane Couette flow or a Taylor Couette flow. Confining walls have different effects on the liquid and the solid phase. Fluid at the wall will behave according to the no-slip and no-penetration boundary conditions, particles at the wall however will only behave according to the no-penetration boundary condition. This means that particles can actually have slip with the walls where the fluid cannot (Jana et al., 1995). Besides that the no-penetration boundary conditions will align particles with the wall promoting a layered structure in the region close to the wall (Yeo & Maxey, 2010a). Numerical simulations of (Gallier et al., 2016) showed that the effect of particle layering in plane Couette flow increases with the particle volume fraction ϕ and reduces with the particle friction factor μ_c. A visualization of one of their simulations is shown in Figure 2-12. For this simulation there is a clear transition from the layered wall region to the chaotic core region. Note that besides the layering in the wall normal direction there also exists a layering in the vorticity direction. The layering in both directions ultimately forms a hexagonal ordering in the plane perpendicular to the sheared plane. Different types of layer structuring can be observed depending on the distance between two confining walls for a specific value of ϕ (Yeo & Maxey, 2010b).

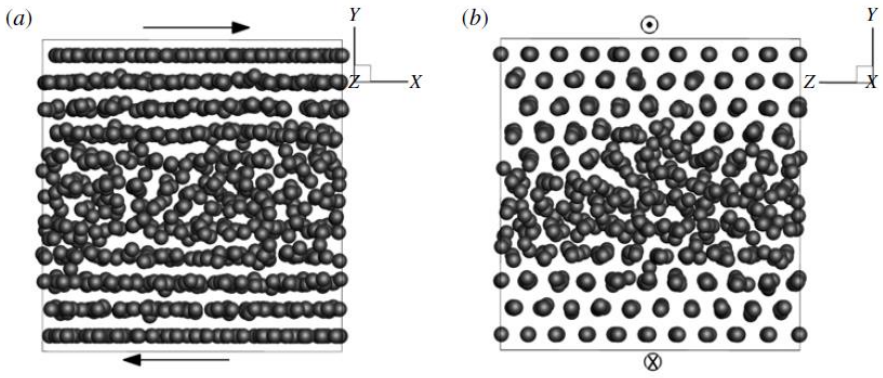

Figure 2-12, Steady-state particle ordering of a confined suspension with $\phi = 0.5$ and $\mu_c = 0$. (a) particle ordering in the sheared plane, (b) particle ordering in the plane perpendicular to the sheared plane. Particle diameters are shown half the actual size for visualization (Gallier et al., 2016). Note: the axis orientations differ from the orientation of the axes in this work.

The viscosity of a confined suspension with strong layering effects is significantly lower than for an unbounded suspensions with the same properties (Gallier et al., 2016). This effect is strong enough to break asymptotic behaviour of suspension viscosity for increasing ϕ as the layering effect also increases with ϕ. Besides that the distance between two confining walls also plays a large role as this allows for different kind of layer orderings. Some results of the relative viscosity for varying wall distances are shown in Figure 2-13 (Yeo & Maxey, 2010b). These results show that the formation of various ordered structures promote different trends for the suspension viscosity.

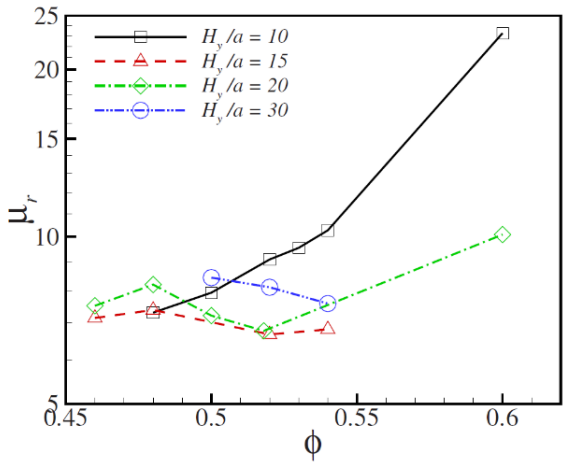

Figure 2-13, The relative viscosity η_r (denoted as μ_r here) as a function of ϕ for different wall separations H_y/a, where a is the particle radius (Yeo & Maxey, 2010b).

Besides the viscosity, confinement of suspensions also affects the normal stresses and therefore the normal stress differences N_1 and N_2. Numerical results show that particle layering promotes positive values for N_1 and an even more negative N_2 as shown in Figure 2-14 (Gallier et al., 2016). This effect can be an explanation for the positive values of N_1 found for some experimental studies on suspension rheology.

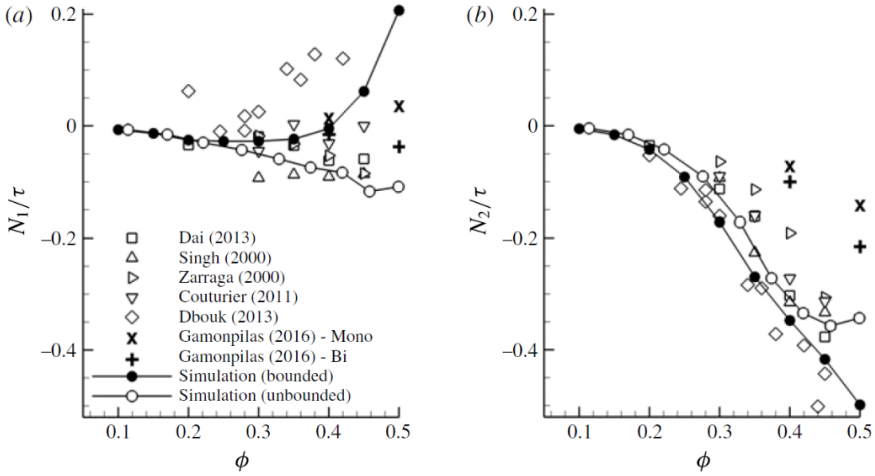

Figure 2-14, The normal stress differences N_1 and N_2 as a function of ϕ for both confined and unbounded suspensions (Gallier et al., 2016).

2.4 Numerical methods

Research with respect to suspension microstructure is generally hard to perform experimentally since suspensions are often opaque. Besides that, it can be difficult and expensive to reach extreme conditions in experimental set-ups. Therefore numerical methods gained a lot of interest in the field of suspension rheology. Numerical simulations provide detailed steady-state or transient flow field data and the possible conditions are less restricted compared to experimental research.

Various numerical methods capable of simulating suspension flow have been developed. Stokesian Dynamics is the most used method, but recently Direct Numerical Simulation (DNS) gained more interest because of the large field of possible applications. DNS is able to produce a fully resolved solution of the flow field at the smallest relevant length scale. For the simulation of suspension this typically implies solving the Navier-Stokes equations for the fluid phase and solving the Newton-Euler equations for the particle phase. Note that no further assumptions are made, which makes this method widely applicable. DNS is capable of simulating arbitrary shaped solid particles, non-Newtonian fluids and high Reynolds number flows. Various DNS methods exist for suspension flows where the main difference is in the coupling between the fluid and the particle phase. At the interface a no-slip and no-penetration boundary condition must be applied, for which multiple approaches exist. Examples are the Immersed Boundary Method (IBM) and the Fictitious Domain Method (FDM). The possibilities with DNS are much less restricted compared to other simulation methods, but the cost of this is that the method is computationally very expensive. Small timesteps are needed to fully resolve all the physics especially for higher Reynolds numbers. However, computational power is increasing rapidly, making DNS more interesting for simulations of suspensions close to the jamming limit.

In this section three numerical methods are discussed in more detail namely: Stokesian Dynamics, Immersed Boundary Method and Fictitious Domain Method.

2.4.1 Stokesian Dynamics

Currently most numerical research on suspensions is performed using Stokesian Dynamics (SD). This is a numerical method that makes use of the approximation $Re_{\dot{\gamma}} = 0$, which linearizes the Navier-Stokes equations. Forces on particles are subdivided in three categories: hydrodynamic forces $\boldsymbol{F}^H$, inter particle forces $\boldsymbol{F}^P$ and Brownian forces $\boldsymbol{F}^B$. The following particle momentum balance can then be constructed (Brady & Bossis, 1988):

$$\boldsymbol{m} \cdot \frac{d\boldsymbol{U}}{dt} = \boldsymbol{F}^H + \boldsymbol{F}^P + \boldsymbol{F}^B, \tag{2.24}$$

with:

$$\boldsymbol{F}^H = -\boldsymbol{R}_{FU}(\boldsymbol{x}^N) \cdot (\boldsymbol{U} - \boldsymbol{U}^\infty) + \boldsymbol{R}_{FE} \cdot \boldsymbol{E}^\infty, \tag{2.25}$$

where $\boldsymbol{R}_{FU}$ and $\boldsymbol{R}_{FE}$ are configuration dependent resistance matrices representing the hydrodynamic force and torque respectively. The inter-particle force $\boldsymbol{F}^P$ can be of any form depending on the contact model. The Brownian force $\boldsymbol{F}^B$ results from thermal fluctuations and is arbitrary by nature. The resistance matrices must be approximated since the amount of particles is typically too large to find an exact solution (Brady & Bossis, 1988). Stokesian Dynamics is not limited to simulation of monodisperse suspensions of spherical particles since the model can be extended to deal with non-spherical or polydisperse suspensions. However a major limitation to the SD method is that it is restricted to Stokes flow, since the assumption $Re_{\dot{\gamma}} = 0$ is in the core of this method. Besides that it's also not possible to simulate suspensions consisting of non-Newtonian fluids using SD.

Simulations of suspensions using SD are able to show reasonable volume fraction dependence and shear thickening behaviour (Ryohei Seto, 2013). However, for a SD solver to show rate dependence an extra force scale must be added. An electrostatic repulsion model proposed by (Mari et al., 2014) gives proper results.

2.4.2 Immersed Boundary Method

The Immersed Boundary Method (IBM) is a two phase simulation method that makes use of a fixed grid (usually Cartesian). Interfaces between the two phases do not necessarily have to coincide with the grid cell boundaries, since boundary conditions are applied by using a forcing method (Mittal & Iaccarino, 2005). The IBM is interesting for the simulation of suspension flow since no regridding will be needed. However, direct numerical simulation of suspension flow typically requires moving boundary conditions. An IBM proposed by (Breugem, 2012) makes use of a Lagrangian grid to define the position of the particle interface, this grid can move freely over the fixed Eulerian grid. The no-slip and no-penetration boundary condition between the two phases is realized by adding a body forcing term to the Navier-Stokes equations at boundary points. This forcing term is computed such that the fluid velocity is equal to the particle surface velocity for every particle (Haeri & Shrimpton, 2012).

Discrete forcing is a method that determines the body forcing term directly from discretization of the Navier-Stokes equations. However the Eulerian and Lagrangian grid points do not coincide, so we need a way to translate velocity and force vectors from one grid to the other. This can be done by using a so-called regularized delta function. This function makes use of the values corresponding to grid points in the neighbourhood and weighs them based on the distance to the grid point of interest. A regularized delta function can be used to interpolate the velocity vectors from the Eulerian grid to the Lagrangian grid, such that the body forcing terms can be computed. After that the body forcing terms can be spread back to the Eulerian grid using the same delta function. This process is visualized in Figure 2-15. The downside of this approach is that during the spreading operation forcing terms will disturb each other. Therefore, the accuracy of this method is improved by a few iterations for computing the forcing terms on the Eulerian grid; this is called a multi-direct forcing scheme (Luo et al., 2007).

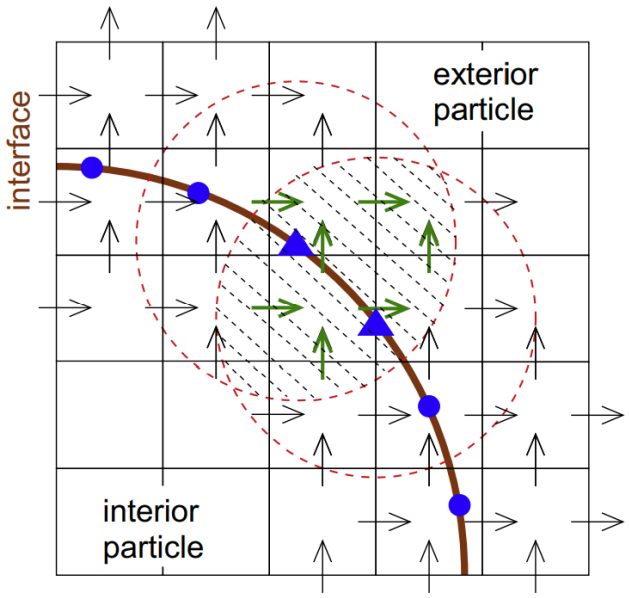

Figure 2-15, Visualization of the interpolation between the Eulerian and the Lagrangian grid. Circles in this figure represent the range of the delta function interpolating between the grids (Breugem, 2012).

Currently the IBM is already applied to identify shear thickening in different flow regimes for varying Reynolds numbers ($Re = 500 - 5000$) in flows for suspensions up to the semi-dilute regime ($\phi \leq 0.3$) (Lashgari et al., 2014). Another study used IBM to research inertial shear thickening for lower Reynolds numbers ($Re = 0.1 - 10$), for the dilute regime (Picano et al., 2013). This study also predicted a volume fraction dependence of the suspension viscosity which is in agreement with Eilers fit for $\phi \leq 0.3$.

2.4.3 Fictitious Domain Method

The Fictitious Domain Method (FDM) is a method for simulating suspension flow using only one grid. In contrast to the IBM, this method only uses an Eulerian grid which is used for both the particle and the fluid phase. Particles are modelled by means of body forces similar to the IBM but here the two phases share the same grid. There is no interpolation and spreading needed in order to apply the boundary conditions for that reason. The forcing method of IBM results in unphysical velocities inside particles which can be a problem in case of flow coupled with heat or mass transfer. However FDM simulates the particles by setting the velocity inside the whole particle equal to the particle velocity instead of only doing this at the boundary, so no unphysical velocities will be present inside the particle (Deen et al., 2014).

A fictitious domain approach was used by (Gallier et al., 2014) in order to simulate the rheology of dense suspensions. Their model contained a contact model that takes the roughness and the friction factor of particles into account. The model was able to predict volume fraction dependence of the suspension viscosity and normal forces that are in agreement with experimental results.

2.5 Discussion

Since the beginning of the 20th century much research has been done with regards to dense suspensions. With the results of numerous rheological experiments correlations have been constructed to predict the behaviour of suspensions. However experimental results do often not agree with each other and the physical understanding to explain those discrepancies is lacking. The rheological behaviour of suspensions is still far from understood, especially in the dense regime.

Experimental research for dense suspensions is often difficult because the substance is normally opaque and besides that extreme conditions are hard to realize in experimental set-ups. Numerical research however is not limited in those ways. Detailed descriptions of suspension flows can be obtained with various available numerical methods. Computational power is a limiting factor, but in the future this will be less of a problem since computational power is increasing continuously. The numerical simulation of suspension flows comes with the challenge of providing a coupling between the fluid and the solid phase. A promising and widely applicable technique that is capable of making this coupling is the Immersed Boundary Method (IBM). This method has proven to be able to predict suspension rheology in the dilute regime (Picano et al., 2013), however simulations of dense suspensions close to the jamming limit using this technique are lacking. The application of the IBM for the simulation of dense suspensions can potentially help understanding the underlaying physics causing non-Newtonian behaviour.

3 Problem statement and objectives

As mentioned in the discussion above the IBM is a promising technique for simulating dense suspensions, however numerical simulations of dense suspensions produced with this technique are lacking. Hence, the following problem statement can be formulated: How accurate is the Immersed Boundary Method for simulating dense suspensions near the jamming limit? The objective of this study will be to validate the capability of the IBM to simulate dense suspensions near the jamming limit by comparing simulation results with available experimental and numerical data. To limit the scope the focus will be on neutrally buoyant non-colloidal suspensions of hard spheres in Stokes flow. Besides that the focus will be on monodisperse suspensions in plane Couette flow.

4 Method

The Immersed Boundary Method will be used to investigate the rheology of suspensions near the jamming condition and to validate the results against available experimental and numerical data. The validation will be performed by comparing the volume fraction and friction factor dependence of the relative viscosity, the normal stress differences and the microstructure. This will be done by using the second-order accurate method from (Breugem, 2012), together with the frictional soft-sphere collision model proposed by (Costa et al., 2015). The solver uses an equidistant staggered Cartesian grid for the fluid phase and a Lagrangian grid for each particle. The governing equations and further details on the numerical method are given below.

4.1 Governing equations

The governing equations for the incompressible fluid phase are the continuity equation and the Navier-Stokes equation:

$$\nabla \cdot \boldsymbol{u} = 0, \tag{4.1}$$

$$\rho_f \left(\frac{\partial \boldsymbol{u}}{\partial t} + \nabla \cdot \boldsymbol{u}\boldsymbol{u} \right) = -\nabla p + \eta_f \nabla^2 \boldsymbol{u} + \rho_f \boldsymbol{f}, \tag{4.2}$$

where $\boldsymbol{u}$ is the fluid velocity, p is the varying contribution to the pressure. ρ_f is the fluid density and μ_f is the fluid viscosity. The force term $\boldsymbol{f}$ is used for imposing boundary conditions at the surface of particles, this will be explained below. To not depend on any units the Navier-Stokes equation is made non-dimensional using the particle diameter d as a length scale, $1/\dot{\gamma}$ as a time scale and $\rho_f d^4 \dot{\gamma}^2$ as a force scale:

$$\frac{\partial \tilde{\boldsymbol{u}}}{\partial \tilde{t}} + \tilde{\nabla} \cdot \tilde{\boldsymbol{u}}\tilde{\boldsymbol{u}} = -\tilde{\nabla}\tilde{p} + \frac{1}{Re_{\dot{\gamma}}} \nabla^2 \tilde{\boldsymbol{u}} + \tilde{\boldsymbol{f}}, \tag{4.3}$$

where $Re_{\dot{\gamma}} = \rho_f d^2 \dot{\gamma} / \eta_f$ and the tilde denotes a dimensionless variable. The governing equations for the particle phase consisting of hard solid spheres is given by:

$$\tilde{\boldsymbol{U}}_p = \tilde{\boldsymbol{u}}_c + \tilde{\boldsymbol{\omega}}_c \times \tilde{\boldsymbol{r}}, \tag{4.4}$$

where $\tilde{\boldsymbol{U}}_p$ is the dimensionless velocity of an infinitesimal particle segment and $\tilde{\boldsymbol{u}}_c$ is the dimensionless particle velocity at the centre of the particle. $\tilde{\boldsymbol{\omega}}_c$ is the dimensionless angular velocity of the particle and $\tilde{\boldsymbol{r}}$ is the dimensionless distance of a point on the particle with respect to the centroid. The translational velocity and the angular velocity are described by the following relations:

$$\frac{1}{6}\pi\rho_r \frac{d\tilde{\boldsymbol{u}}_c}{d\tilde{t}} = \oint_{\partial V} \tilde{\boldsymbol{\tau}} \cdot \boldsymbol{n} d\tilde{A} + \tilde{\boldsymbol{F}}_c, \tag{4.5}$$

$$\frac{1}{60}\pi\rho_r \frac{d\tilde{\boldsymbol{\omega}}_c}{d\tilde{t}} = \oint_{\partial V} \tilde{\boldsymbol{r}} \times (\tilde{\boldsymbol{\tau}} \cdot \boldsymbol{n}) d\tilde{A} + \tilde{\boldsymbol{T}}_c, \tag{4.6}$$

where $\rho_r = \rho_p / \rho_f$ is the density ratio. The stress tensor for a Newtonian fluid is given by $\tilde{\boldsymbol{\tau}} = -\tilde{p}\boldsymbol{I} + (1/Re_{\dot{\gamma}})(\nabla\tilde{\boldsymbol{u}} + \nabla\tilde{\boldsymbol{u}}^T)$ and $\boldsymbol{n}$ is the outward pointing normal vector at the particle surface. Inter particle contact is given by $\tilde{\boldsymbol{F}}_c$ and $\tilde{\boldsymbol{T}}_c$ representing the dimensionless force and the torque resulting from the contact interaction.

At the surface of a particle the no slip and no penetration boundary condition must be applied. This implies that $\tilde{\boldsymbol{u}} = \tilde{\boldsymbol{U}}_p(\boldsymbol{X})$ at every point $\boldsymbol{X}$ at the surface. For the IBM this boundary condition is imposed using the force term $\tilde{\boldsymbol{f}}$ in the governing equation of the fluid phase.

Similar to the governing equations all further references to physical quantities in this work are dimensionless. For visual clearance however the tilde accents are not shown on the variables in the sequel.

4.2 Numerical method

The solver makes use of a low storage 3-step Runge-Kutta scheme for discretization of all terms except for the pressure gradient, that term is discretized using a Crank-Nicolson scheme. Simulation of the fluid phase is performed according to the following pressure-correction scheme (Breugem, 2012):

$do\ q = 1,3$

$$\boldsymbol{u}^{*} = \boldsymbol{u}^{q-1} + \frac{\Delta t}{\rho_f}\left(-\left(\alpha_q + \beta_q\right)\nabla p^{q-\frac{3}{2}} + \alpha_q \boldsymbol{rhs}^{q-1} + \beta_q \boldsymbol{rhs}^{q-2}\right)$$

$$\boldsymbol{u}^{**} = \boldsymbol{u}^{*} + \Delta t \boldsymbol{f}^{q-\frac{1}{2}}$$

$$\nabla^2 \tilde{p} = \frac{\rho_f}{(\alpha_q+\beta_q)\Delta t}\nabla \cdot \boldsymbol{u}^{**}$$

$$\boldsymbol{u}^{q} = \boldsymbol{u}^{**} - \frac{(\alpha_q+\beta_q)\Delta t}{\rho_f}\nabla \tilde{p}$$

$$p^{q-\frac{1}{2}} = p^{q-\frac{3}{2}} + \tilde{p}$$

$end\ do$

The constants are given by: $\alpha_1 = \frac{32}{60}, \beta_1 = 0, \alpha_2 = \frac{25}{60}, \beta_2 = -\frac{17}{60}, \alpha_3 = \frac{45}{60}$ and $\beta_3 = -\frac{25}{60}$. This scheme consists of three sub steps where $q = 0$ corresponds to the previous time level and $q = 3$ corresponds to the new time level. The first prediction $\boldsymbol{u}^{*}$ is made by using terms from previous time steps, then this prediction is used to determine the forcing term $\boldsymbol{f}$ in order to impose the boundary conditions at the surface of particles. The forcing term $\boldsymbol{f}$ is determined with a multi-direct forcing scheme (Breugem, 2012). This forcing scheme interpolates the fluid velocity $\boldsymbol{u}^{*}$ to the Lagrangian grid to determine $\boldsymbol{U}_l^{*}$ such that the forcing term $\boldsymbol{F}_l$ can be determined. This term is defined on the Lagrangian grid so it must be spread back to the Eulerain grid to determine $\boldsymbol{f}$. During the spreading operation the imposed boundary condition of different Lagrangian nodes will interfere with each other resulting in disturbances in the boundary condition. For that reason these interpolation and spreading operations are repeated N_s times to improve the accuracy of the forcing terms around the particles. After that a second prediction $\boldsymbol{u}^{**}$ is made by including the forcing term, this prediction is used to determine the Poisson equation for the correction pressure $\tilde{p}$. This Poisson equation is solved efficiently using an FFT-based solver. The particle motion is discretized within the same loop with the same Runge-Kutta scheme. The translational and angular velocity of the particles are determined taking hydrodynamic and contact forces into account. For the fluid phase a staggered equidistant Cartesian grid is used, the finite volume method is applied for discretization and spatial derivatives are estimated using central differencing.

4.3 Contact model

Forces on particles as a result of mechanical contact are determined using a soft sphere collision model (Costa et al., 2015). The contact behaviour in this model is based on three parameters: the sliding friction factor μ_c, the normal coefficient of restitution $e_{n,d}$ and the tangential coefficient of restitution $e_{t,d}$. The coefficients of restitution are defined as the loss of momentum during a collision:

$$e_{n,d} = \frac{u_{out,n}}{u_{in,n}}, \tag{4.7}$$

$$e_{t,d} = \frac{u_{out,t}}{u_{in,t}}. \tag{4.8}$$

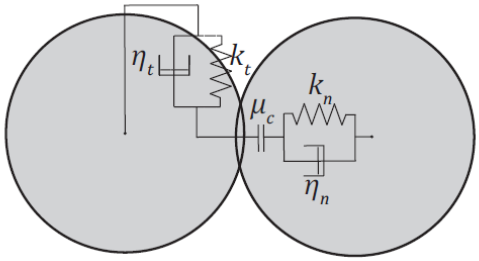

Figure 4-1, Schematic view of the soft sphere collision model (Costa et al., 2015).

Contact forces from a particle j on a particle i are separated in a normal component $\boldsymbol{F}_{ij,n}$ and a tangential component $\boldsymbol{F}_{ij,t}$. Both components are determined by considering a spring dashpot system schematically shown in Figure 4-1. The normal force is determined with:

$$\boldsymbol{F}_{ij,n} = -k_n \boldsymbol{\delta}_{ij,n} - \eta_n \boldsymbol{u}_{ij,n}, \tag{4.9}$$

where $\boldsymbol{\delta}_{ij,n}$ is the particle overlap in the normal direction and $\boldsymbol{u}_{ij,n}$ is the relative velocity in the normal direction. The normal spring coefficient k_n and damping coefficient η_n are given by:

$$k_n = \frac{m_e\left(\pi^2 + \ln^2 e_{n,d}\right)}{(N\Delta t)^2}, \tag{4.10}$$

$$\eta_n = -\frac{2m_e \ln e_{n,d}}{(N\Delta t)}, \tag{4.11}$$

where $m_e = \left(m_i^{-1} + m_j^{-1}\right)^{-1}$ is the reduced mass and $N\Delta t$ is the duration of the collision. The collision time is usually stretched such that the model resolves the collision well even with large time increments Δt. The tangential force is determined with:

$$\boldsymbol{F}_{ij,t} = \min\left(\left|\left|-k_t \boldsymbol{\delta}_{ij,t} - \eta_t \boldsymbol{u}_{ij,t}\right|\right|, \left|\left|-\mu_c \boldsymbol{F}_{ij,n}\right|\right|\right) \boldsymbol{t}_{ij}, \tag{4.12}$$

where $\boldsymbol{\delta}_{ij,t}$ is the tangential displacement and $\boldsymbol{u}_{ij,t}$ is the relative tangential velocity. The tangential spring coefficient k_t and damping coefficient η_t are given by:

$$k_t = \frac{m_{e,t}\left(\pi^2 + \ln^2 e_{t,d}\right)}{(N\Delta t)^2}, \tag{4.13}$$

$$\eta_t = -\frac{2m_{e,t} \ln e_{t,d}}{(N\Delta t)}, \tag{4.14}$$

where $m_{e,t} = m_e\left(1 + \frac{1}{K^2}\right)^{-1}$ is the reduced mass of the tangential system with $K^2 = 2/5$ the normalised particle radius of gyration for a sphere. The determination of the tangential force takes

into account the transition between stick and slip, therefore it's important to update the tangential displacement according to the right contact conditions:

$$\boldsymbol{\delta}_{ij,t}^{*n+1} = \boldsymbol{R} \cdot \boldsymbol{\delta}_{ij,t}^{n} + \int_{t^n}^{t^{n+1}} \boldsymbol{u}_{ij,t} dt, \tag{4.15}$$

$$\boldsymbol{\delta}_{ij,t}^{n+1} = \begin{cases} \boldsymbol{\delta}_{ij,t}^{*n+1} & , \left|\left|\boldsymbol{F}_{ij,t}\right|\right| \leq \mu_c \left|\left|\boldsymbol{F}_{ij,n}\right|\right| \ (stick) \\ \left(\frac{1}{k_t}\right)\left(-\mu_c \left|\left|\boldsymbol{F}_{ij,n}\right|\right| \boldsymbol{t}_{ij} - \eta_t \boldsymbol{u}_{ij,t}\right) & , \left|\left|\boldsymbol{F}_{ij,t}\right|\right| > \mu_c \left|\left|\boldsymbol{F}_{ij,n}\right|\right| \ (slip) \end{cases}, \tag{4.16}$$

where $\boldsymbol{R}$ is a rotation tensor which is used to update the orientation of the tangential displacement. The total contact force and torque can then be determined with:

$$\boldsymbol{F}_{ij}^{c} = \boldsymbol{F}_{ij,t} + \boldsymbol{F}_{ij,n}, \tag{4.17}$$

$$\boldsymbol{T}_{ij}^{c} = \frac{d}{2}\left(\boldsymbol{n}_{ij} \times \boldsymbol{F}_{ij,t}\right). \tag{4.18}$$

4.4 Lubrication correction

Prior to mechanical contact between solid bodies large lubrication forces may be present. When the gap between two solid bodies is large enough the IBM is able to resolve the lubrication forces well. But as the bodies come closer to each other the spatial resolution gets too coarse to resolve the steep profile of the lubrication forces. For that reason a lubrication correction is applied when the particle gap ε is smaller than $\varepsilon_{\Delta x}$ (Costa et al., 2015). As the particle gap reduces even further at some point the particle roughness is expected to play a role as explained in section 2.2.4. These roughness effects are simulated by assuming that the *effective* gap width remains constant and is equal to ε_σ when $0 \leq \varepsilon < \varepsilon_\sigma$, where ε_σ is the roughness height. A schematic overview of this separation in close particle interactions is given in Figure 4-2.

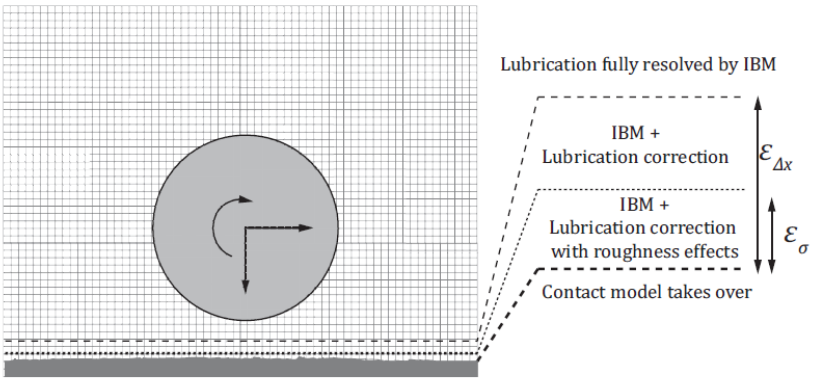

Figure 4-2, Schematic overview of the contact model for different gap widths ε (Costa et al., 2015).

5 Simulations

For this study a beam-shaped domain is used, as shown in Figure 5-1. The x, y and z directions correspond to the vorticity, the velocity and the velocity gradient direction respectively. The domain lengths are set to $L_x = 13.5$, $L_y = 27$ and $L_z = 13.5$. An opposing velocity is prescribed on the top and the bottom walls to simulate a plane Couette flow and in addition the no-penetration and no-slip boundary conditions are applied to simulate the effect of confinement. The wall velocities are related to the particle Reynolds number with:

$$Re_{\dot{\gamma}} = \frac{\rho_f d^2 \dot{\gamma}}{\eta_f}, \tag{5.1}$$

$$\dot{\gamma} = \frac{v_{top} - v_{bottom}}{L_z}. \tag{5.2}$$

Note that all variables are made dimensionless with the particle diameter d, the shear rate $\dot{\gamma}$ and the fluid density ρ_f. As a result the dimensionless shear rate is given with $\dot{\gamma} = 1$ such that $v_{top} = L_z/2$ and $v_{bot} = -L_z/2$. In this study we are interested in Stokes flow, so a low Reynolds number is necessary. However, setting the Reynolds number extremely low is not practical, because as a result particles will barely move and therefore it will be computationally expensive to gain statistically independent results. For this study the flow parameters are defined such that the Reynolds number is equal to $Re_{\dot{\gamma}} = 0.1$, as a result the fluid viscosity is equal to $\eta_f = 10$. The domain is periodic in the x and y-direction and the length L_y was chosen such that the particle distribution is able to decorrelate over this length.

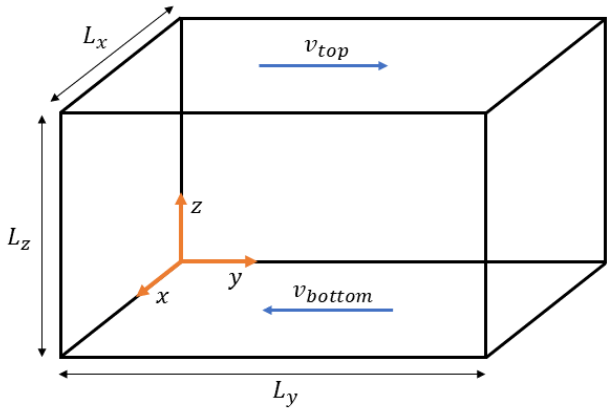

Figure 5-1, A schematic view of the simulated domain.

For this study we chose to vary both the particle volume fraction ϕ and the coefficient of sliding friction μ_c. Friction coefficients for particle-particle and particle-wall contact are always equal to each other in this work. The range of particle volume fractions is set from $\phi = 0.2 - 0.6$ with increments of 0.1 and all these volume fractions are simulated with a friction factor of both 0 and 0.39. This value of $\mu_c = 0.39$ for frictional particles is based on yet unpublished tilted-flume experiments on an immersed bed of polystyrene spheres conducted by M.T. Shajahan, TU Delft. The normal coefficient of restitution is defined as $e_{n,d} = 0.97$, which can be considered realistic according to experimental results (Joseph & Hunt, 2004), and the tangential coefficient of restitution is defined as $e_{t,d} = 0.1$, which is lower than experimental results typically show. This value of $e_{t,d}$ is chosen lower to promote sliding behaviour in mechanical contact; the degree of solid friction is thus mostly controlled by μ_c in our simulations. The particle roughness is set to $\epsilon_\sigma = 0.004$, which is a reasonable value for particles of $O(1)$ mm in diameter with a surface roughness of $O(1)$ micrometer (Joseph et al., 2001).

5.1 Initial particle positions

An effective method for particle initialisation is to use a random number generator to determine the initial particle positions. After every particle placement a routine can check if there is no overlap with the walls or with other particles. This method works well for suspensions with a particle volume fraction of $\phi \leq 0.3$, but for larger ϕ this method is not able to find enough free space in order to reach the desired amount of particles. For that reason another particle position initialisation is used for the cases with $\phi > 0.3$. With a structured ordering it is possible to reach significantly higher concentrations. Here we choose for a body-centred crystalline structure, as shown in Figure 5-2. This structured ordering allows for a maximum particle volume fraction of $\phi \approx 0.68$ in case of an unbounded flow.

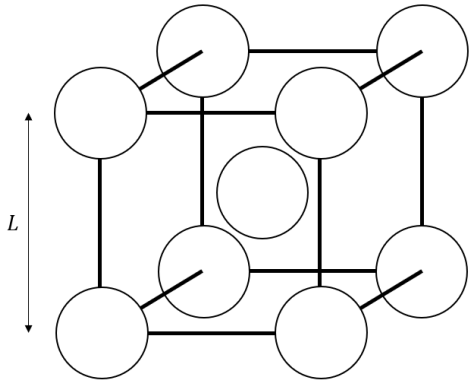

Figure 5-2, Body-centred crystalline structure

The sides of this cubic structure has equal lengths L. As L gets smaller ϕ increases until the spheres overlap in the diagonal direction, which we cannot allow. Therefore the diagonal of the cubic structure must always be larger than two particle diameters: $2d \leq \sqrt{3L^2}$ (or: $L \geq 2d/\sqrt{3}$). The routine sets L initially too large and then decreases it slowly until the point at which the amount of particles that fit in the domain N is larger than or equal to the desired amount of particles $N_{desired}$. The routine works in the following way:

$while\ N < N_{desired}$

$$N_x = floor\left(\frac{L_x}{L}\right),\ N_y = floor\left(\frac{L_y}{L}\right),\ N_z = floor\left(\frac{2L_z}{L}\right) - 1$$

$$N = N_x \cdot N_y \cdot N_z$$

$$L = L - 0.001$$

where N_x, N_y and N_z are the amount of particles in the x, y and z direction respectively, the body-centred particles are only counted in the z-direction. Note that L is normalised with the particle diameter d. The amount of particles N increases with large discrete steps as L decreases, so when the while loop is done N is probably too large. This allows us to increase the randomness of the particle initialization by random removal of particles from the domain till $N = N_{desired}$. After that there is still some space to perturb the particle positions within this structure, which allows us to increase the randomness of the particle initialization even further.

5.2 Convergence

For the simulations to converge the spatial and temporal resolutions must both be fine enough. The Eulerian grid is equidistant with: $\Delta x = \Delta y = \Delta z = 1/16$ and the Lagrangian grid is made up of 746 surface segments for every particle. The temporal increment is constrained to the physical time scale more than to the numerical scheme and is set to $\Delta t = 1.5625 \cdot 10^{-3}$. This value is found empirically.

Convergence of every individual simulation is checked using the forces that both the particle phase and the fluid phase exert on the walls. These forces can be subdivided in a tangential contribution and a normal contribution. The tangential forces on the walls contribute to the shear stress and indicate how well the simulation is converged for the viscosity. This shear stress can be determined for the bottom wall with:

$$\sigma_{yz,bot} = \frac{1}{L_x L_y} \sum_x \sum_y f_{t,p-w}(x,y) + \frac{1}{Re_{\dot{\gamma}}} \frac{v_f(x,y,\Delta z/2) - v_f(x,y,0)}{\Delta z/2}, \tag{5.3}$$

where $f_{t,p-w}$ contains the tangential contact forces that acts from a particle on the wall. The shear stress on the top wall can be determined in a similar way. The normal forces on the walls are also of interest, as they give an indication of how well the simulation is converged for the particle stress in the wall-normal direction. For the bottom wall the normal stress can be determined with:

$$\sigma_{zz,bot} = \frac{1}{L_x L_y} \sum_x \sum_y f_{n,p-w}(x,y) + p(x,y,0), \tag{5.4}$$

where $f_{n,p-w}$ contains the normal contact forces that act from a particle on the wall. Both bottom wall stresses are plotted as a function of the dimensionless time t in Figure 5-3 for the frictionless cases. All cases start with a fast increasing transient followed by a much slower decreasing transient. At the very first time step particles do not make contact with the walls due to the way particle positions are initialized. The flow is initialised with a linear velocity profile for both fluid and particles as if the mixture behaves like single-phase flow. Immediately at the start of a simulation, the flow will rapidly adjust to the presence of the solid particles, which explains the rapid increase in both the tangential and normal wall stress at $t = 0$. This is then followed by a slower adjustment of the initial particle configuration to the flow. The gradual increase in normal stress for the lower concentrations can be explained by the gradual increase in particle-wall collision events and accompanying adjustment of the wall pressure as initially particles do not make contact with the walls. A transient time t_{trans} can be defined by judging both stresses for every case. This part of the simulation can be excluded from the total simulated time to analyse the steady-state behaviour. The values of t_{trans} and the simulated steady-state time t_{steady} are given in Table 1.

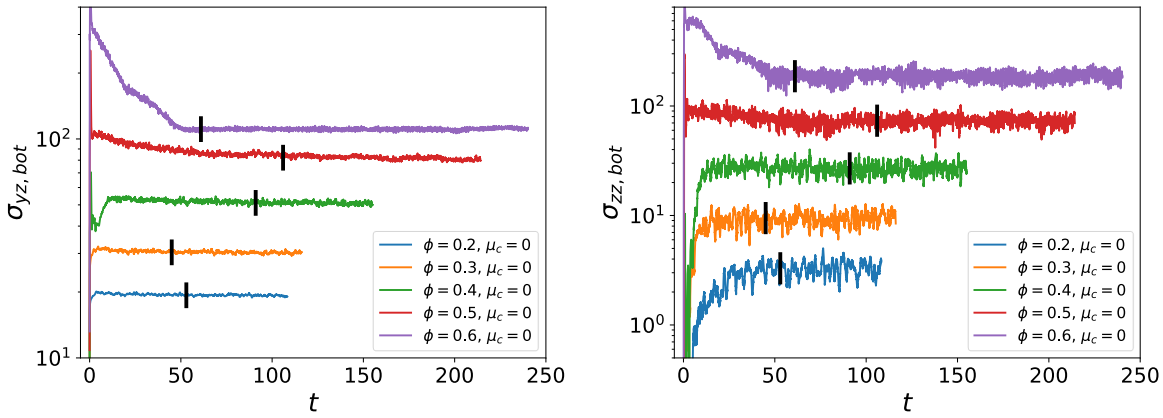

Figure 5-3, The bottom wall shear stress $\sigma_{yz,bot}$ and the bottom wall normal stress $\sigma_{zz,bot}$ as a function of the dimensionless time t for the frictionless cases with $\phi = 0.2, 0.3, 0.4$ and 0.5. The vertical bars indicate the end of the transient t_{trans}.

μ_c	0					0.39				
ϕ	0.2	0.3	0.4	0.5	0.6	0.2	0.3	0.4	0.5	0.6
t_{trans}	53	45	91	106	61	68	53	76	91	140
t_{steady}	51	67	59	102	162	51	42	38	61	78

Table 1, The duration of the transient t_{trans} and the amount of simulated steady-state time t_{steady} for every case.

6 Postprocessing

Several postprocessing routines make it possible to interpret the generated data. In this section a detailed explanation about the postprocessing routines is given.

6.1 Superficial averages

The numerical method used in this work produces detailed 3-dimensional velocity and concentration fields. For a plane Couette flow however we can expect the statistical flow properties not be constant in the velocity and the vorticity direction. The only statistical variations of velocity, stress or concentration will be present in the velocity gradient direction. For that reason it is useful to determine superficial plane averaged flow properties, providing the flow parameters as a function of the wall-normal position z. The superficial averages for the velocity can be determined with:.

$$\langle \boldsymbol{u}_f \rangle(z) = \frac{1}{L_x L_y} \sum_x \sum_y \boldsymbol{u}_f(x,y,z)\big(1-\alpha(x,y,z)\big)\Delta x \Delta y, \tag{6.1}$$

$$\langle \boldsymbol{u}_p \rangle(z) = \frac{1}{L_x L_y} \sum_x \sum_y \boldsymbol{u}_p(x,y,z)\alpha(x,y,z)\Delta x \Delta y, \tag{6.2}$$

where α is the solid phase indicator function (computed from the solid volume fraction inside a computational grid cell using a level-set approach). This function can also be used to determine the particle volume fraction as a function of the wall-normal position:

$$\langle \phi \rangle(z) = \frac{1}{L_x L_y} \sum_x \sum_y \alpha(x,y,z)\Delta x \Delta y. \tag{6.3}$$

Intrinsic averages can then be determined with:

$$\langle \boldsymbol{u}_f \rangle^f(z) = \frac{\langle \boldsymbol{u}_f \rangle(z)}{1-\langle \phi \rangle(z)}, \tag{6.4}$$

$$\langle \boldsymbol{u}_p \rangle^p(z) = \frac{\langle \boldsymbol{u}_p \rangle(z)}{\langle \phi \rangle(z)}. \tag{6.5}$$

Superficial and intrinsic averages will also be averaged over time to obtain nicely converged data. These time averaged properties will be annotated with a bar accent like $\langle \overline{\boldsymbol{u}}_f \rangle$ for example.

6.2 Pair distribution function

The pair distribution function $g(\boldsymbol{r})$ gives the probability of finding another particle at a specific point $\boldsymbol{r}$ with respect to a randomly selected base particle, as already mentioned in section 2.2.4. To construct this function the volume of interest must be subdivided in a finite amount of volume segments. Volume segments must be significantly smaller than the particle volume $V_{seg} \ll V_p$ in order to obtain a high resolution. After that the pair distribution function can be determined with:

$$g(\boldsymbol{r}) = \frac{\left(V_{total}/V_{seg}\right)}{N(N-1)} \sum_p \sum_{p_d} \delta\left(\boldsymbol{r} - \left(\boldsymbol{x}_{p_d} - \boldsymbol{x}_p\right)\right), \tag{6.6}$$

where $\boldsymbol{x}_p$ is the centroid position of a base particle, $\boldsymbol{x}_{p_d}$ is the centroid position of the other particle in a pair. The function δ returns 1 if the particle is in the segment volume of interest, otherwise 0 is returned as visualized in Figure 6-1. The summation in equation (6.6) is normalised with the probability of finding a particle in the volume segment in case of a perfect homogeneous distribution, such that $g(\boldsymbol{r}) \approx 1$ for large $\boldsymbol{r}$. Here V_{total} is the total domain volume, V_{seg} is the segment volume and N is the total amount of particles. This function can be determined for a

series of time samples, such that the average can be determined in order to obtain a better a converged plot.

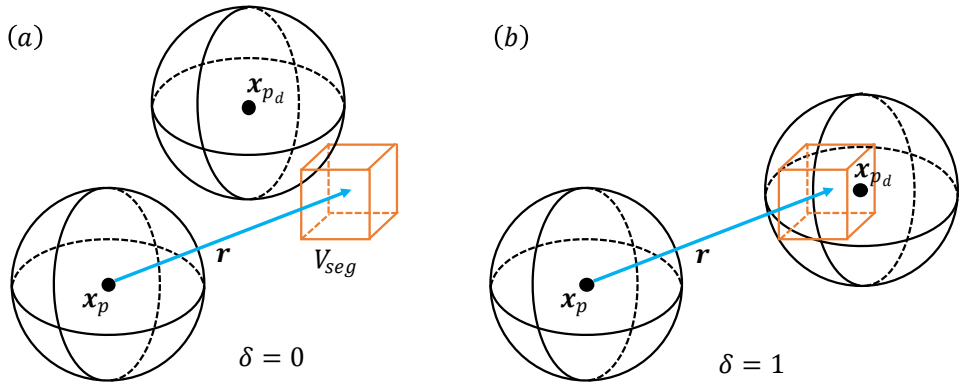

Figure 6-1, Schematic view of how the δ-function works. The function returns 1 if the second particle in a duo finds itself in the volume of interest V_{seg} (b), otherwise 0 is returned (a).

6.3 Particle stress tensor

Particles suspended in a fluid will exert additional stresses $\boldsymbol{\sigma}_p$ that contribute to the mixture model stress tensor $\boldsymbol{\sigma}$ as explained in section 2.2.2. The components of the particle stress tensor for a specific particle s can be related to the stresslet and the torque with:

$$\sigma^s_{p,ij} = \frac{6}{\pi}\left(S_{ij} + T_{ij}\right), \tag{6.7}$$

where the stresslet S_{ij} and the torque T_{ij} represent the symmetric and the asymmetric part of the first moment of traction over the particle surface respectively. Since the particles can rotate freely no torque can exist on the particles, such that $T_{ij} = 0$. Therefore only the symmetric part S_{ij} exists, and as a result $\sigma^s_{p,ij} = \sigma^s_{p,ji}$. The stresslet can be determined with:

$$S_{ij} = \int_{V_p} f_i x_j dV \approx \sum_l F_i x_j, \tag{6.8}$$

where F_i is the i-component of a force acting on the particle and x_j is the j-component of the distance between the particle centroid and the element on which the force acts. The summation in equation (6.8) is made over all Lagrangian elements of a particle l. From section 2.2.1 we know that a sheared flow field can be decomposed in a rotating motion and a stresslet, Figure 6-2 gives the streamlines of a stresslet around a single particle in the yz-plane. In this figure it is visible how the presence of the particle disturbs the shearing motion. The disturbance of the flow field results in additional stresses in the fluid that are balanced by stresses in the particle, trying to deform the particle. Deformations of the particle will be negligibly small however, since the Youngs modulus of the solid phase is high enough to consider it rigid. Besides hydrodynamic forces also collisional forces can contribute to the stresslet acting on a particle. In the case of collisional forces on a particle the sum of both contributions still forms a particle stress tensor with only a symmetric part.

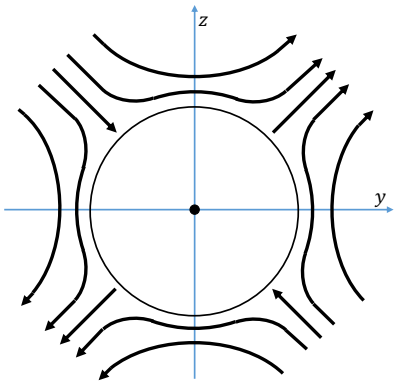

Figure 6-2, Streamlines of the stresslet acting on a single particle.

The particle stress is determined for every individual particle and originates from both hydrodynamic and collisional forces. For a specific particle s we can state for the average stress within a particle:

$$\sigma_{p,ij}^{s} = \sigma_{p,ij}^{hyd} + \sigma_{p,ij}^{col}. \tag{6.9}$$

The hydrodynamic contribution in equation (6.9) can be estimated by:

$$\sigma_{p,ij}^{hyd} = \frac{6}{\pi}\left(S_{ij}^{hyd} - \sum_{e_{in}} \sigma_{ij}^{int} \Delta x \Delta y \Delta z \right), \tag{6.10}$$

$$S_{ij}^{hyd} = -\sum_{l} x_j F_i^{IBM} + \sum_{l} x_j F_i^{lub}, \tag{6.11}$$

where F_i^{IBM} is the hydrodynamic force as a result of the IBM, F_i^{lub} is the hydrodynamic force as a result of the lubrication correction. The internal fluid stress from the artificial fluid within the particle σ_{ij}^{int} is added here as a correction on the contribution from the IBM forces. The summation variables l and e_{in} stand for the Lagrangian and internal Eulerian grid cells respectively. The collisional contribution in equation (6.9) is estimated by:

$$\sigma_{p,ij}^{col} = \frac{6}{\pi} S_{ij}^{col}, \tag{6.12}$$

$$S_{ij}^{col} = \sum_{l} x_j F_i^{col}, \tag{6.13}$$

where F_i^{col} is the collisional force. Note that particles cannot pull on each other by means of mechanical contact so $\boldsymbol{F}^{col}$ can never point out of the particle surface. As a result the collisional contributions to the normal stresses $\sigma_{p,xx}^{col}, \sigma_{p,yy}^{col}$ and $\sigma_{p,zz}^{col}$ can only be negative.

We can determine the superficial particle stress in the volume as a function of the wall normal direction z with:

$$\langle \sigma_{p,ij} \rangle (z) = \frac{1}{L_x L_y} \sum_{s=1}^{N} \sum_{x,y} \sigma_{p,ij}^{s}\, \alpha(x,y,z,s) \Delta x \Delta y, \tag{6.14}$$

where the solid phase indicator function α indicates the specific particle s in this case. Note that $\sigma_{p,ij}^{s}$ is the average particle stress for the particle s. This averaging step simplifies the post processing as it is complicated to determine the actual heterogeneous stress distribution within

the particle. However, as a result the particle stress profiles $\langle\sigma_{p,ij}\rangle(z)$ can show artificial fluctuations near the walls where the solid volume fraction rapidly varies in the wall-normal direction due to particle layering. When the complete particle stress tensor is known the normal stress differences and the particle pressure can be determined with the following relations:

$$\langle N_1\rangle = \langle\sigma_{p,yy}\rangle - \langle\sigma_{p,zz}\rangle, \tag{6.15}$$

$$\langle N_2\rangle = \langle\sigma_{p,zz}\rangle - \langle\sigma_{p,xx}\rangle, \tag{6.16}$$

$$\langle p_p\rangle = -\frac{1}{3}\big(\langle\sigma_{p,xx}\rangle + \langle\sigma_{p,yy}\rangle + \langle\sigma_{p,zz}\rangle\big). \tag{6.17}$$

Using the particle stress, the relative viscosity can be computed from equation (2.11) according to:

$$\eta_r = 1 + \frac{\langle\sigma_{p,yz}\rangle}{\frac{1}{Re_{\dot\gamma}}\frac{\partial\langle v_m\rangle}{\partial z}}, \tag{6.18}$$

where $\langle v_m\rangle = \langle v_p\rangle + \langle v_f\rangle$ is the streamwise mixture velocity. Note that in the channel core $\partial\langle v_m\rangle/\partial z$ generally deviates from 1, the shear rate imposed on the walls.

7 Results

In this section the simulation data is analysed in order to determine the rheological behaviour. To give a first impression on how the particles are distributed in the domain, cross sections of the yz and xz-planes are given in Figure 7-1 and Figure 7-2 for the frictional cases of $\phi = 0.5$ and 0.6 respectively. For the frictional case of $\phi = 0.5$ particles close to the walls clearly tend to align with the walls. This layering effect seems to propagate into the domain over the length of at least 2 particle diameters. Further from the walls the particles show a more random distribution, however particles do seem to form chains along the compressional axis of the flow.

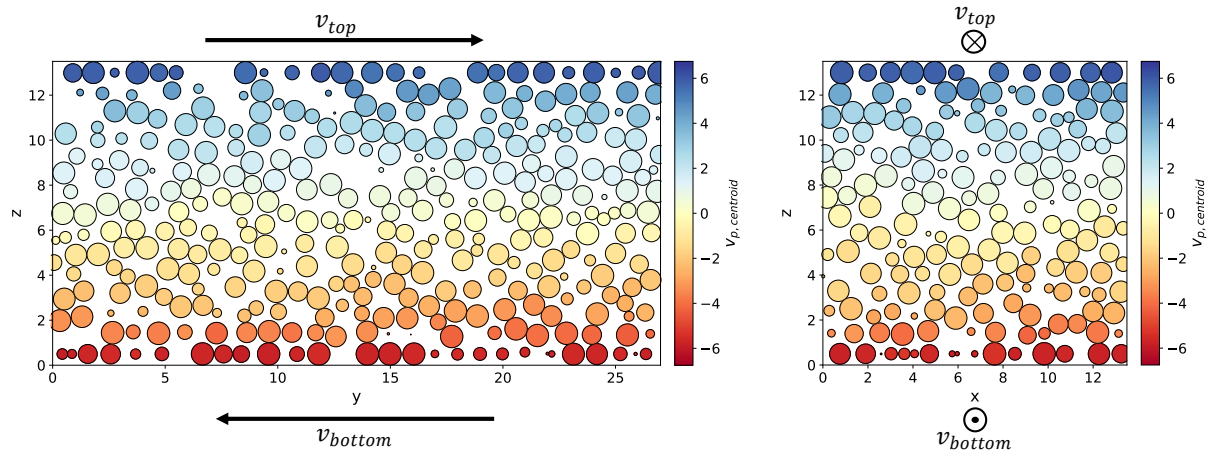

Figure 7-1, Cross sections in the yz-plane (left) and the xz-plane (right) for the frictional case of $\phi = 0.5$. Colours in this plot indicate magnitude of the particle centroid velocity $v_{p,centroid}$.

The particles form the frictional case of $\phi = 0.6$ in Figure 7-2 show a significantly more ordered distribution. Not only is the wall-induced particle layering visible throughout the whole domain in the yz-plane, also the cross section in the xz-plane shows strong ordering. A hexagonal structure has formed in the complete domain with layers of particles moving over each other.

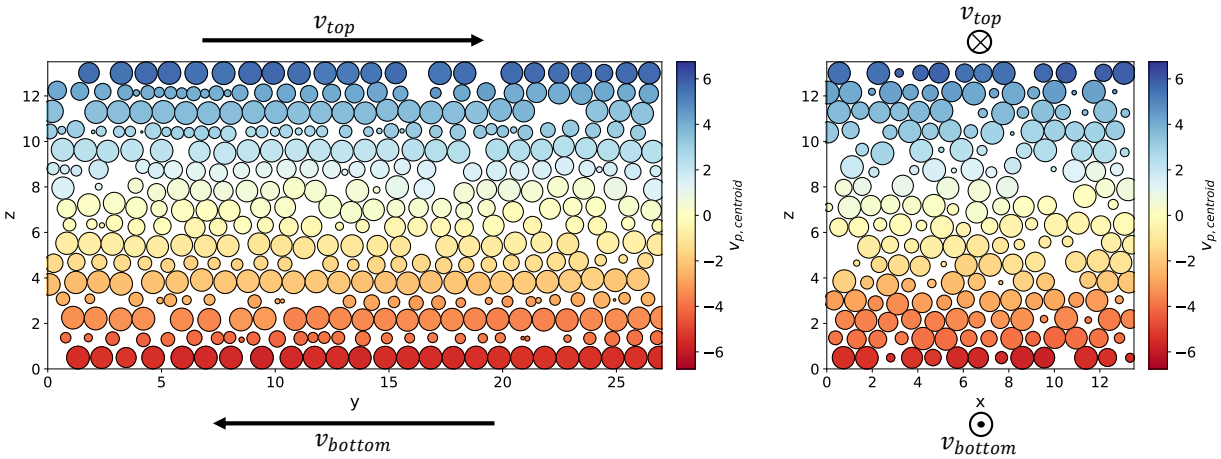

Figure 7-2, Cross sections in the yz-plane (left) and the xz-plane (right) for the frictional case of $\phi = 0.6$. Colours in this plot indicate magnitude of the particle centroid velocity $v_{p,centroid}$.

In the sequel of this section the rheological properties of the simulated suspensions are analysed in terms of the microstructure, the viscosity and the normal particle stresses. All results are obtained by applying the postprocessing steps from section 6 to the steady-state data of the simulated cases.

7.1 Stress budgets

The superficial averages of the velocities and the particle stresses can be used to analyse the stress budgets in the streamwise and the wall-normal direction. For the streamwise direction the total shear stress can be computed with:

$$\langle \bar{\sigma}_{yz} \rangle = \frac{1}{Re_{\dot{\gamma}}} \frac{d\langle \bar{v}_m \rangle}{dz} + \langle \bar{\sigma}_{p,yz} \rangle, \tag{7.1}$$

where the first term is the viscous shear stress with $\langle \bar{v}_m \rangle = \langle \bar{v}_p \rangle + \langle \bar{v}_f \rangle$ the mixture velocity and the second term is the particle shear stress. As there is no imposed pressure gradient, the total shear stress should be constant and equal to the total wall shear stress when the suspension microstructure is the same in the entire channel. Both stress budget terms are plotted as a function of the wall-normal position z for the frictional case of $\phi = 0.4$ in Figure 7-3. From this plot it is clear that for this case the particle shear stress has the largest contribution to the total shear stress in the streamwise direction. Besides that some wall-effects are visible, however do note that the fluctuations are artificial to some extend as particle stresses are averaged first over the individual particle volumes before computing the superficial volume average. The average total shear stress at the walls $\frac{1}{2}\left(\langle \bar{\sigma}_{yz,bot} \rangle + \langle \bar{\sigma}_{yz,top} \rangle\right)$ is also plotted for comparison, where the particle wall shear stress was computed from the average tangential contact force per unit wall area. It is clear that this average wall shear stress is not completely representative for the shear stress in the core of the domain, reflecting the difference in suspension microstructure between the core and the wall regions.

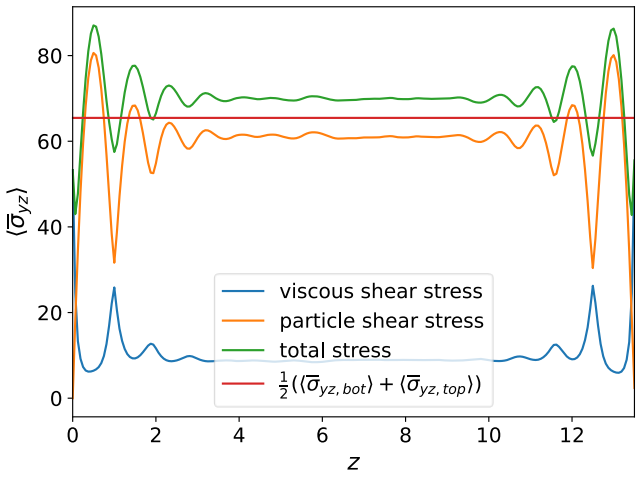

Figure 7-3, Stress budgets for the streamwise direction for the frictional case of $\phi = 0.4$. Plotted along with average total wall shear stress.

For the wall-normal direction the total stress can be computed with:

$$\langle \bar{\sigma}_{zz} \rangle = -\langle \bar{p}_f \rangle + \langle \bar{\sigma}_{p,zz} \rangle, \tag{7.2}$$

where the first term is the fluid pressure and the second term is the normal particle stress in the wall-normal direction. As for the total shear stress, also the total wall-normal stress is expected to be constant in height and equal to wall stress values when the suspension microstructure would be homogeneous. Both stress contributions form equation (7.2) are plotted in Figure 7-4 as a function of the wall-normal position for the frictional case of $\phi = 0.4$. Also for the wall-normal direction it is clear that the particle stress has a much higher contribution to the total stress. The total stress can be compared to the total average normal stress at the walls $\frac{1}{2}\left(\langle \bar{\sigma}_{zz,bot} \rangle + \langle \bar{\sigma}_{zz,top} \rangle\right)$.

Again, as for the total shear stress, also the total wall-normal stress deviates significantly from the wall values in the core region.

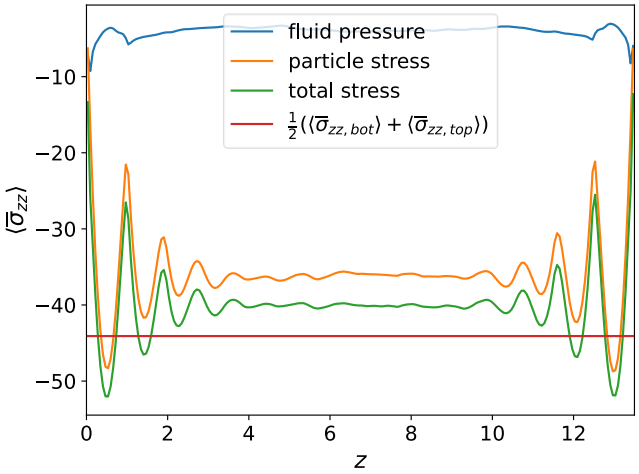

Figure 7-4, Stress budgets for the wall-normal direction for the frictional case of $\phi = 0.4$. Plotted along with average total wall shear stress.

It is clear that the walls have a significant effect on the stress budgets and therefore we cannot expect to make an accurate estimate of the suspension rheology by only considering stresses at the walls. This same conclusion is made in the numerical work of (Gallier et al., 2016) and (Yeo & Maxey, 2010a) and also in the experimental work of (Jana et al., 1995). Note however that most experimental research in this field makes use of rheometers which actually do determine the suspension rheology based on measurements at the walls.

7.2 The effect of confinement

From the previous section we know that the stress budgets near the walls deviate significantly from the rest of the domain due to particle layering. To visualize the particle layering effect the time-averaged superficial concentration profiles for both the frictionless and the frictional cases are given in Figure 7-5.

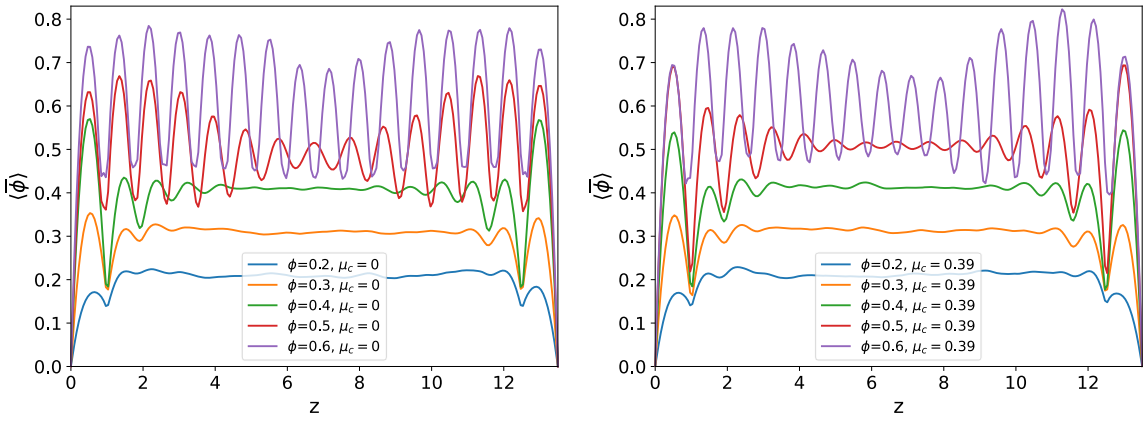

Figure 7-5, Concentration profiles: without friction (left) and with friction (right)

The concentration profiles show a particle layering effect for all cases. Suspensions with higher particle volume fractions show thicker particle layering regions, where the most dense suspensions show layering throughout the whole domain. Comparison between the frictionless and the frictional cases shows that friction reduces the layering effect. These observations are in line with the results of (Gallier et al., 2016). Interestingly, the wavelength of the oscillations in the

concentration decreases near the maximum packing limit. For example the number of oscillation is 15 for $\phi = 0.5$ but 16 for $\phi = 0.6$ for both the frictional and the frictionless cases.

For further investigation of the simulation data it is convenient to make a distinction between the wall region and the core region for every individual case. This can be done by defining a wall-normal thickness L_{wall} that will be excluded from the complete domain when analysing the core region. The value of L_{wall} for every case is given in Table 2. Note that the most dense cases of $\phi = 0.5$ and 0.6 show particle layering throughout the complete domain, nevertheless a core region has been defined in order to analyse the effect of particle layering in the core. For these cases L_{layer} is chosen such that no bias is present as a result of the layered distribution. The cases with $\phi \leq 0.4$ show a particle volume fraction near the walls that is lower than the average since the particles cannot overlap with the walls. As a result the particle volume fraction in the core ϕ_{core} is a few percent higher than the average. Interestingly, the cases with $\phi \geq 0.5$ show the opposite effect. The layered particle distribution is very dense close to the walls for these cases, while this packing tends to become more chaotic towards the core of the channel. This relatively chaotic packing in the core allows for a lower particle volume fraction in the core such that ϕ_{core} is lower than the average for these cases. Because of the differences in packing, ϕ_{core} is used instead of ϕ for analysis of the core region.

μ_c	0					0.39				
ϕ	0.2	0.3	0.4	0.5	0.6	0.2	0.3	0.4	0.5	0.6
L_{wall}	5.5	5.5	5.5	5.75	5.95	5.5	5.5	5.5	5.85	5.95

Table 2, The value of L_{wall} for every case.

Confinement also has an effect on the velocity profiles as shown in

Figure 7-6. The boundary conditions have different effects on both phases a stated before in section 2.3. We can see that the fluid phase has no slip with the walls while the particle phase does have slip. Besides that, both velocity profiles deviate slightly from the linear Couette flow profile near the walls, where in the core region a linear profile is established again. Apart from the wall layers, the intrinsic fluid and particle velocity profiles coincides (no macroscopic slip between the phases). Note furthermore that the shear rate in the core $\dot{\gamma}_{core}$ is a few percent lower than the average shear rate $\dot{\gamma}$. As a result the Reynolds number in the core $Re_{\dot{\gamma}_{core}} = \rho_f d^2 \dot{\gamma}_{core} / \eta_f$ is also lower than $Re_{\dot{\gamma}}$.

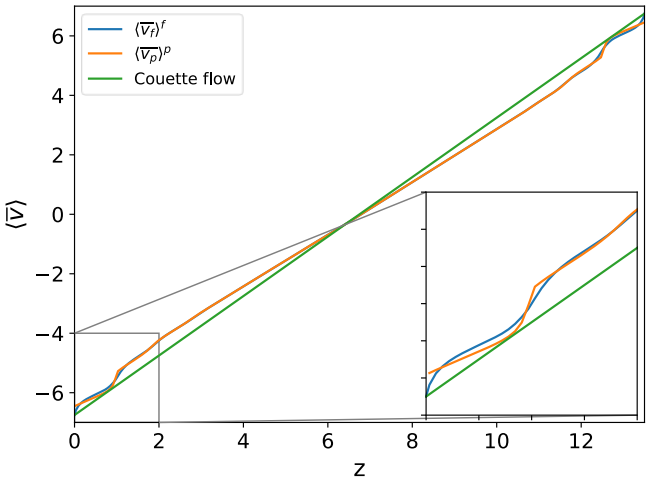

Figure 7-6, Time-averaged intrinsic velocity profiles for the frictional case of $\phi = 0.4$.

7.3 Microstructure

Suspension rheology is governed by particle interactions in the microstructure. To understand the origin of differences in rheological behaviour as a result of changes in ϕ or μ_c it is useful to look for differences in the microstructure. Pair distribution functions give insight in the relative ordering of particles, which tells much about the microstructure. The post processing routine from equation (6.6) makes it possible to determine the pair distribution function for different kinds of volume segments.

7.3.1 Microstructure in the core region

Pair distribution functions in the yz-plane for the core regions of the frictional cases are shown in Figure 7-7. Corresponding 3-dimensional pair distribution functions $g(|\boldsymbol{r}| < 1.05)$ are shown in Figure 7-8. For the most dilute case of $\phi = 0.2$ there already exists a slight for-aft asymmetry which is the result of irreversible mechanical contact between the particles. As a result the low probability zones that exist because of lubrication forces are slightly tilted from the y-axis. For the more dense cases the probability of finding another particle centroid at around $1d$ distance increases and the high probability zone rotates in the anticlockwise direction. This same trend was observed in the experimental work of (Blanc et al., 2013).

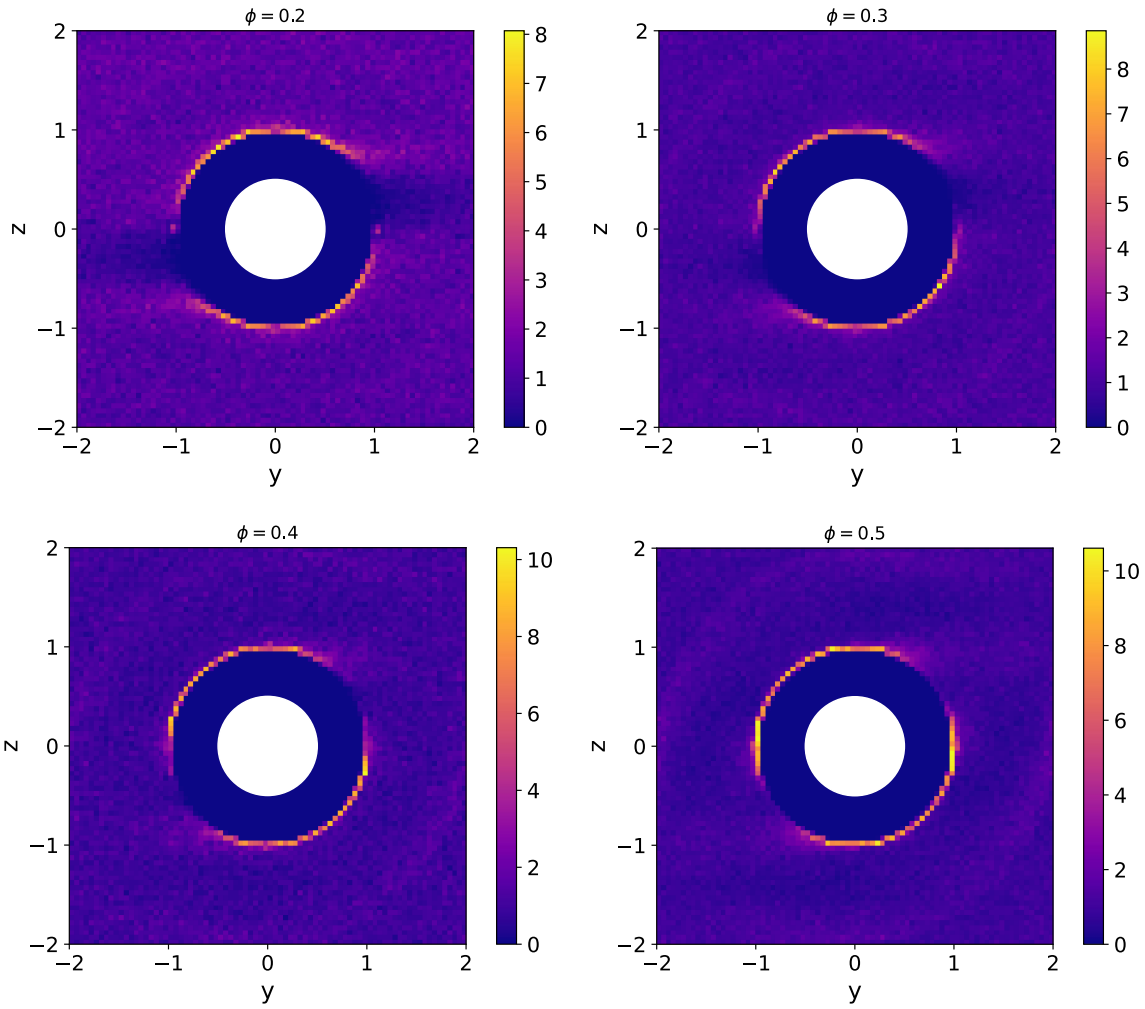

Figure 7-7, Pair distribution functions in the yz – plane for $\phi = 0.2, 0.3, 0.4$ and 0.5 with $\mu_c = 0.39$.

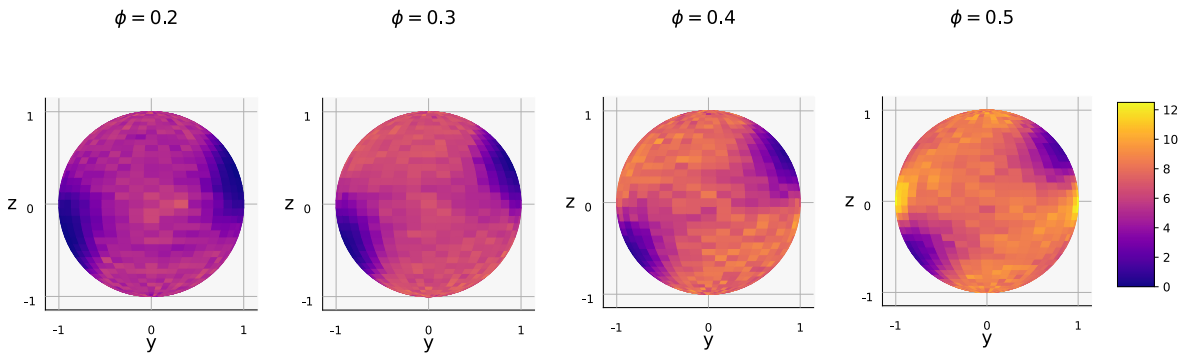

Figure 7-8, 3-dimensional pair distribution function $g(|\boldsymbol{r}| < 1.05)$ for $\phi = 0.2, 0.3, 0.4$ and 0.5 with $\mu_c = 0.39$.

A quantitative comparison between the current results and results from literature is shown in Figure 7-9. This figure gives the pair distribution function $g(|\boldsymbol{r}| < 1.05)$ in the yz-plane along the upper half of the particle surface as a function of θ, where θ is the angle with the negative y-axis in the clockwise direction. The same curve exists for the bottom half of the particle due to symmetry over the xy-plane. The current results are in good agreement with the numerical results from (Gallier et al., 2014) and (Yeo & Maxey, 2010a). Lower friction factors seem to result in a higher peak near $\theta = 0$, while the probability of finding a particle near $\theta = \pi/4$ reduces.

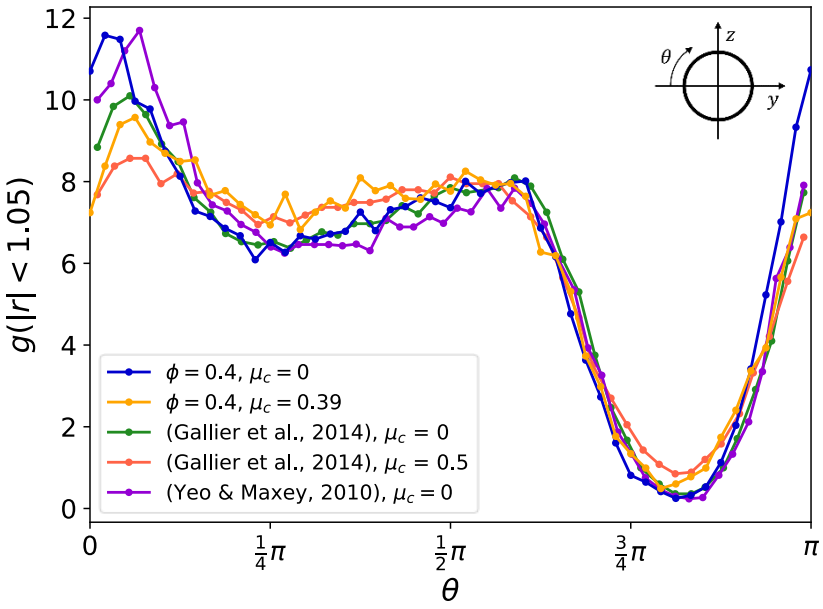

Figure 7-9, Pair distribution function $g(|\boldsymbol{r}| < 1.05)$ for the core region of the cases with $\phi = 0.4$. Plotted together with results of (Gallier et al., 2014) and (Yeo & Maxey, 2010a).

7.3.2 Microstructure of the wall region

The microstructure in the wall regions can be analysed with the same postprocessing tools, however this time we only consider the particles that find themselves in a certain region close to one of the walls. In Figure 7-10 the pair distribution functions are given for particles that find themselves in the region defined by: $z_2 - 0.25 < z_2 < z_2 + 0.25$, where z_2 is the wall-normal position of the second particle layer from the bottom wall. From this result we can clearly see that for the more dense suspensions particle layering is stronger and reaches further into the domain.

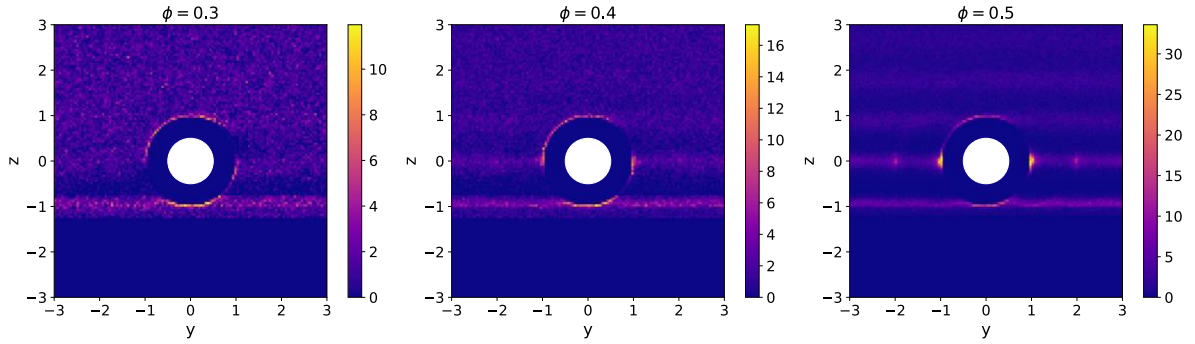

Figure 7-10, Pair distribution functions in the yz-plane for particles near the bottom wall: $z_2 - 0.25 < z_2 < z_2 + 0.25$, where z_2 is the wall-normal position of the second particle layer from the bottom wall. Results are shown for the frictional cases of $\phi = 0.3, 0.4$ and 0.5.

A direct comparison of the pair distribution functions in the wall region with results of (Yeo & Maxey, 2010a) is given in Figure 7-11. Similar to Figure 7-9 this plot gives the pair distribution function $g(|\boldsymbol{r}| < 1.05)$ as a function of θ in the yz −plane. Slight differences exist between both results, but for the largest part a good agreement exists.

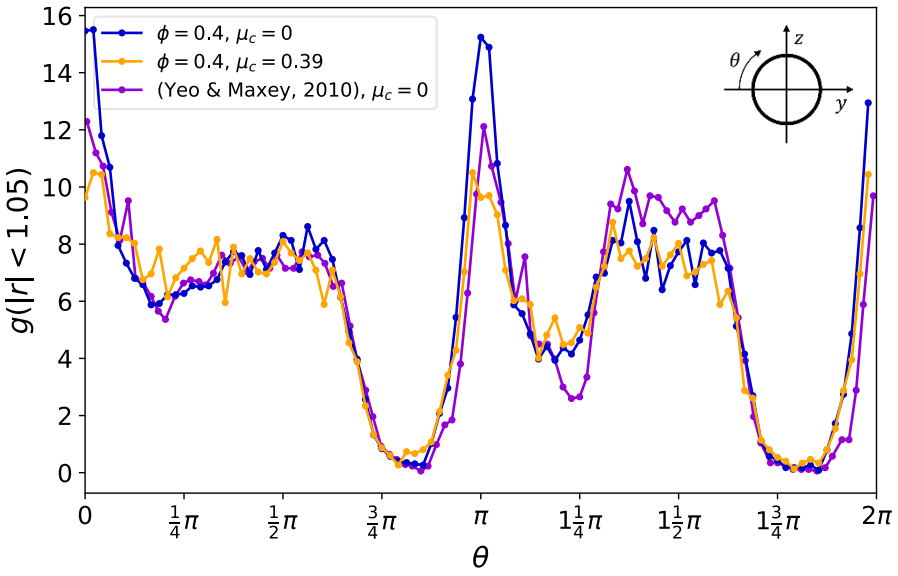

Figure 7-11, Pair distribution function $g(|\boldsymbol{r}| < 1.05)$ for the bottom wall region (defined by $1 < z < 2.5$) of the cases with $\phi = 0.4$. Plotted together with results of (Yeo & Maxey, 2010a).

Besides layering in the wall-normal direction there also exists a layered structure in the vorticity direction. This second layering effect is visible in Figure 7-12, where the pair distribution functions near the walls of frictionless cases is given for the xz-plane. From this results it becomes clear that for $\phi > 0.4$ a hexagonal structure tends to form near the walls. Similar to the wall-normal layering also this layering effect is stronger for larger values of ϕ, which is in-line with

observations from (Yeo & Maxey, 2010b). For both the frictionless and the frictional case of $\phi = 0.6$ this hexagonal structure can be found throughout the whole domain. Note that the concentration profiles of Figure 7-5 show 15 and 16 layers in the wall-normal direction for frictionless cases of $\phi = 0.5$ and $\phi = 0.6$ respectively. This means that the average layer height is smaller than 1 particle diameter, since the channel is only 13.5 particle diameters high. This is also a result of the hexagonal ordering near the walls. The fact that there is 1 layer difference between the two cases can be a result of the hexagonal structure being present throughout the whole domain for $\phi = 0.6$, which allows for a higher layer density. One could argue that this hexagonal structure is an artefact of the particle initialization, this is not the case however. The initial particle positions formed a cubic lattice with additional body-centred particles, the current structure however is clearly not cubic shaped anymore. So significant reordering has taken place.

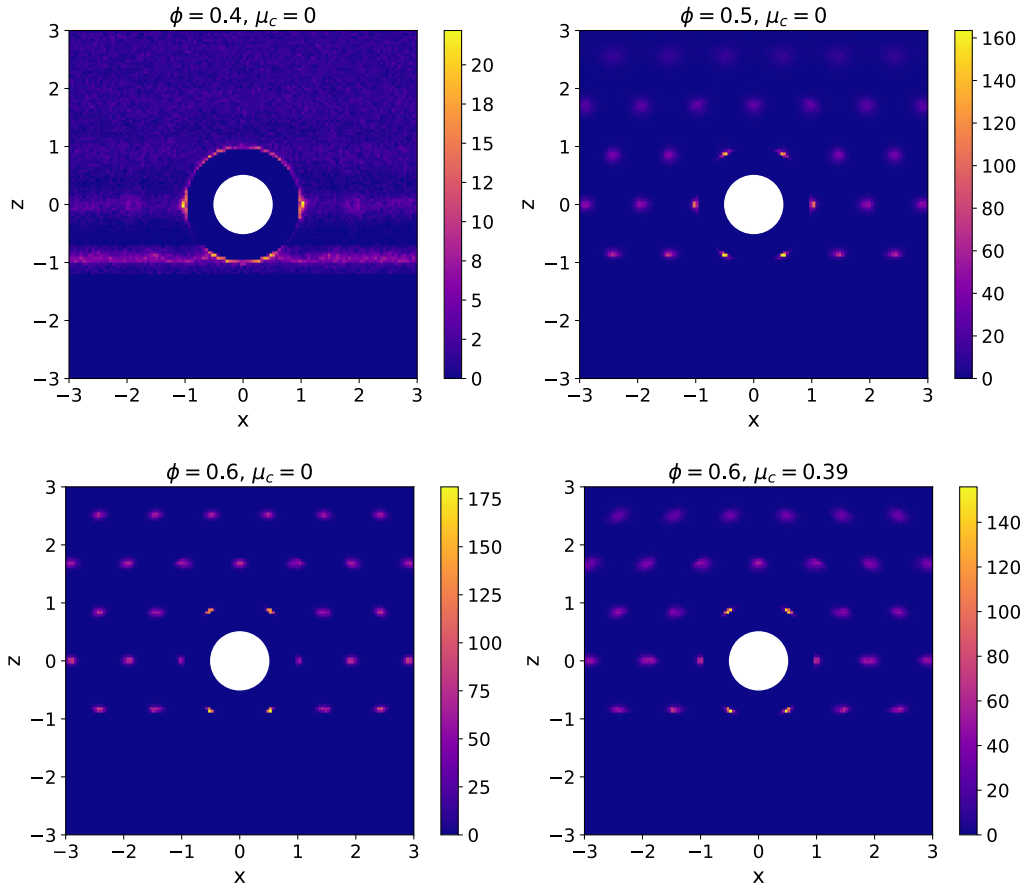

Figure 7-12, Pair distribution functions in the xz-plane for particles near the bottom wall: $z_2 - 0.25 < z_2 < z_2 + 0.25$, where z_2 is the wall-normal position of the second particle layer from the bottom wall. Results are shown for the frictionless cases $\phi = 0.4, 0.5$ and 0.6 and for the frictional case of $\phi = 0.6$.

7.4 Viscosity

Determining the viscosity in a plane Couette flow is relatively straightforward since the shear stress is usually constant for the complete domain. For confined suspensions however particle layering effects will alter the shear stresses close to the walls. Therefore the core region is analysed separately from the complete domain in this section.

7.4.1 Viscosity in the core region

The relative viscosity in the core region $\eta_{r,core}$ can be determined with equation (6.14) by making use of the particle shear stress averaged over the core region. The resulting viscosities are plotted in Figure 7-13 as a function of ϕ for both the frictional and the frictionless cases. The results for the frictionless cases agree well with the frictionless results of (Gallier et al., 2014) and (Yeo & Maxey, 2010a). The frictional case shows a steeper incline, which is also in agreement with the observations of (Gallier et al., 2014). Experimental results from (Zarraga et al., 2000) and (Dbouk et al., 2013) show even steeper dependencies, which suggests that their particles had even higher friction factors. Note that the values of the relative viscosity for the most dense cases are lower than could be expected based on the asymptotic trend for the more dilute cases, which is a result of particle layering in the core region. This decrease in relative viscosity as a result of particle layering is also observed in the work of (Gallier et al., 2016) and (Yeo & Maxey, 2010b).

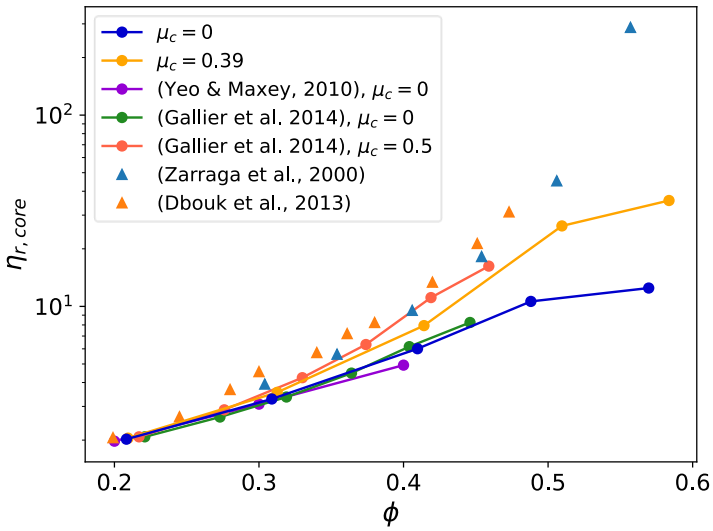

Figure 7-13, Relative viscosity η_r for the core region as a function of ϕ. Plotted together with other numerical results (●) (Yeo & Maxey, 2010a), (Gallier et al., 2014) and experimental results (▲) (Zarraga et al., 2000), (Dbouk et al., 2013)

A decomposition of the relative viscosity in a collisional and a hydrodynamic contribution is given in Figure 7-14. From this decomposition we can see that for frictional particles the hydrodynamic contribution is dominating for $\phi \lesssim 0.4$. More dense frictional suspensions show a rapidly increasing collisional contribution to the relative viscosity. For the frictionless cases this rapid increase in the collisional contribution is not observed, the reason for this can be that we have not simulated dense enough frictionless cases with an un-layered core region. The hydrodynamic contribution seems to be more or less unaffected by changes in the friction factor. From the

decreased steepness in the trend of η_r^{col} for the most dense cases it is clear that this contribution is responsible for the deviation from the asymptotic trend observed in Figure 7-13.

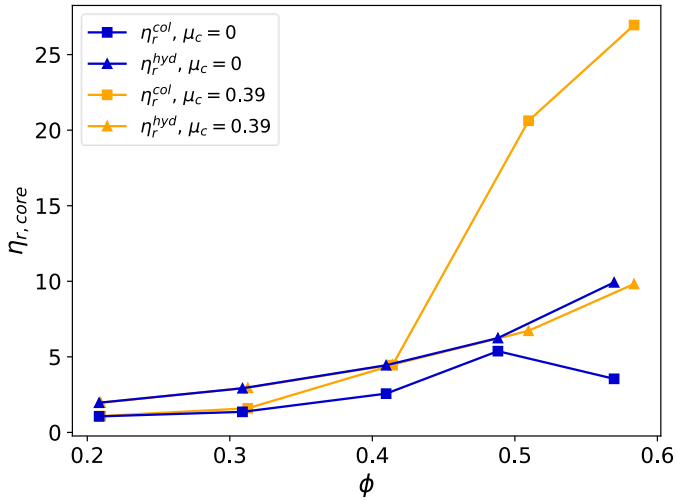

Figure 7-14, Decomposition of the relative viscosity for the core region $\eta_{r,core}$ in a collisional (■) and hydrodynamic contribution (▲) for both the frictionless and the frictional cases.

The maximum packing fraction ϕ_m for both the frictionless and the frictional cases can be estimated by fitting the values for all ϕ with a least square error method to a known correlation. In this work we chose to fit the data to the Marron & Pierce equation, $\eta_r = (1 - \phi/\phi_m)^{-2}$ (Maron & Pierce, 1956). In order to find ϕ_m for unlayered suspensions the frictionless cases with $\phi \geq 0.5$ and the frictional case of $\phi = 0.6$ have been excluded here. For the frictionless particles a maximum packing fraction of $\phi_m = 0.69$ was found and for the frictional particles $\phi_m = 0.635$ was found. The relative viscosity as a function of the normalised particle volume fraction ϕ/ϕ_m is given in Figure 7-15 together with numerical and experimental results from literature. From this plot it is clear that all results collapse on the same line. The maximum packing fraction for the frictionless cases is close to the value found for the data of (Gallier et al., 2016), which is $\phi_m = 0.685$. For the same work a maximum packing fraction of $\phi_m = 0.61$ was found for frictional cases. This is lower than the value found for the frictional cases in this work, which is a result of the higher friction factor. The maximum packing fraction for the frictionless cases of (Yeo & Maxey, 2010a) is estimated as $\phi_m = 0.725$, which is significantly higher compared to the value found in this work. Both experimental data sets show a lower jamming limit: $\phi_m = 0.59$ for (Zarraga et al., 2000) and $\phi_m = 0.575$ for (Dbouk et al., 2013). The reason for this difference in experimental and numerical results for ϕ_m can be a difference in the friction factor as mentioned before. Another reason could be slightly non-spherical particles in experimental set-ups, which is likely to be the case to some extent.

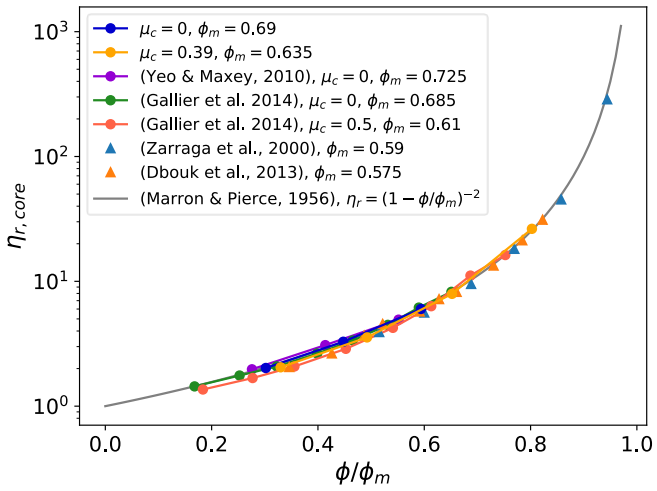

Figure 7-15, The relative viscosity in the core $\eta_{r,core}$ as a function of the normalised particle volume fraction ϕ/ϕ_m. Plotted together with other numerical results (●) (Yeo & Maxey, 2010a), (Gallier et al., 2014) and experimental results (▲) (Zarraga et al., 2000), (Dbouk et al., 2013)

7.4.2 Viscosity of a confined suspension

The effect of particle layering on the particle shear stress $\sigma_{p,yz}$ and its contributions is shown in Figure 7-16 for the frictional case of $\phi = 0.5$. The shear stress contributions are more or less constant in the core region but in the wall regions both contributions deviate significantly. The collisional contribution is lower in the wall regions compared to the core region. This difference can be explained by the difference in particle pair orientations. For the core region particles are likely to make contact in the complete compressional quadrants as shown in Figure 7-7, while in the wall regions particles are most likely to make contact in the y and z-direction as shown in Figure 7-10. In contrast to the collisional contribution the hydrodynamic contribution to the shear stress increases close to the walls.

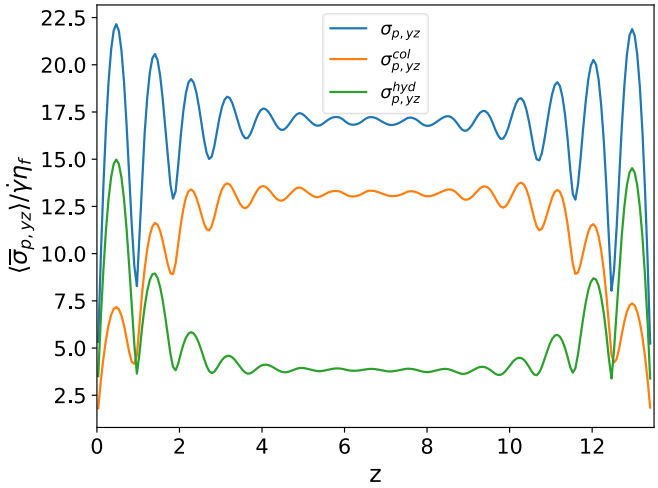

Figure 7-16, The particle shear stress $\langle\bar{\sigma}_{p,yz}\rangle$ normalised with $\dot{\gamma}\eta_f$ (the shear stress for a single phase fluid flow) as a function the wall normal position z for $\phi = 0.5$ and $\mu_c = 0.39$. The particle shear stress is decomposed in a collisional part $\sigma^{col}_{p,yz}$ and a hydrodynamic part $\sigma^{hyd}_{p,yz}$.

As we know from section 7.2 the layered structure tends to extend further into the domain for increasing ϕ. Therefore we can expect the relative viscosity for the total domain to deviate more from the relative viscosity in the core for higher ϕ. To visualise this effect the contributions to the relative viscosity of the frictional cases are plotted in Figure 7-17 as a function of ϕ for both the

core region and the total domain. It is clear that the effect on the hydrodynamic contribution is negligible. The effect on the collisional contribution is significant however, especially for the largest values of ϕ. Collisional contributions to the relative viscosity are responsible for it going to infinity at ϕ_m as already mentioned in the previous section. Particle layering, however, reduces the relative viscosity such that the asymptotic trend is broken. From section 7.4.1 we know that particle layering also alters the relative viscosity in the core region in a similar way for the most dense cases. Note that in Figure 7-17 even these cases show significantly higher collisional contributions to the relative viscosity for the core region compared to the total domain. This indicates that for those cases particle interactions close to the walls and in the core are not the same despite the layering effect being present in both regions. The total relative viscosity for the complete domain is given in Figure 7-18, plotted together with results from (Gallier et al., 2016) and (Yeo & Maxey, 2010a). The results are in good agreement with both datasets for $\phi \leq 0.5$. But for the cases with $\phi = 0.6$ the current results do not predict the same dampened trend as shown by (Gallier et al., 2016). Note, however that a different channel height is used for those results and from results of (Yeo & Maxey, 2010b) it is clear that the relative viscosity is highly dependent on the channel height for suspensions with $\phi \gtrsim 0.5$.

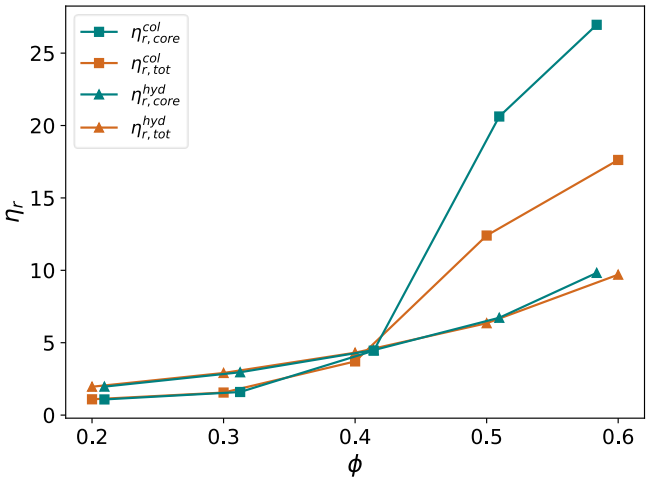

Figure 7-17, The collisional (■) and hydrodynamic contributions (▲) to the relative viscosity η_r for both the core region and the total domain as a function of ϕ for the frictional cases.

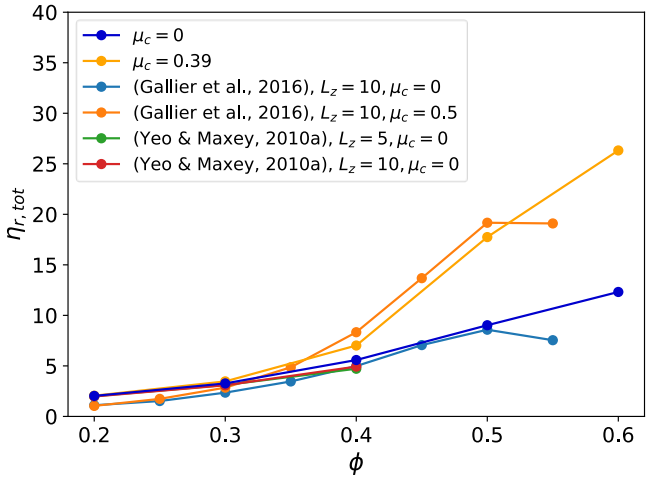

Figure 7-18, The relative viscosity $\eta_{r,tot}$ for the total domain as a function of ϕ for both the frictionless and the frictional cases. Plotted together with results from (Gallier et al., 2016) and (Yeo & Maxey, 2010a).

7.5 Normal particle stresses

In this section the normal particle stresses will be discussed for both the core region and for the total domain. The normal particle stresses are given by the diagonal components of the particle stress tensor that can be obtained with the relations given in section 6.3.

7.5.1 Normal particle stresses in the core region

Particle stresses in the core can be determined by averaging equation (6.14) over the core region. Both the normal particle stresses and the particle pressure are plotted as a function of ϕ in Figure 7-19. The stresses are normalised with the total shear stress in the core:

$$\tau_{core} = \eta_{r,core} \frac{1}{Re_{\dot{\gamma}}} \frac{\dot{\gamma}_{core}}{\dot{\gamma}}$$

From these results it is clear that the normal particle stresses are always negative in all directions. The frictionless cases are in reasonable agreement with the results of (Gallier et al., 2014). The frictional cases are not directly comparable with the results from literature because different friction factors are used, the same steepening trend is observed for an increasing friction factor however. Results for the particle pressure p_p are also in agreement with results from (Gallier et al., 2014). Interestingly, the only normal particle stress showing a significant variation in trend as a result of the particle layering effect in the core for the most dense cases is $\sigma_{p,yy}$. The particles in this layered structure tend to form chains of particles with more or less the same velocity oriented in the y-direction as shown in Figure 7-2. Therefore the collisional contribution to $\sigma_{p,yy}$ is significantly reduced. The normal particle stress $\sigma_{p,xx}$ also deviates from the asymptotic trend, but to a lesser extend than $\sigma_{p,yy}$. In contrast $\sigma_{p,zz}$ seems to not deviate from the asymptotic trend at all.

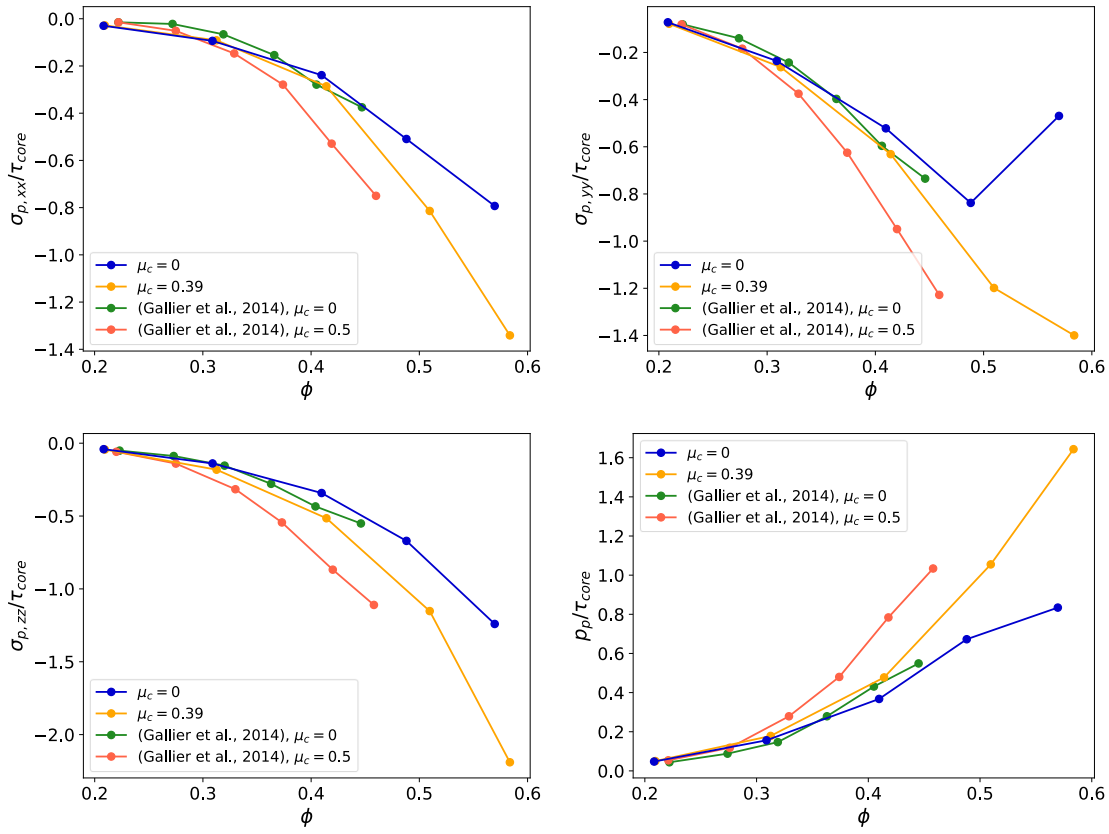

Figure 7-19, Core region particle stresses in the x, y and z directions and the particle pressure, decomposed in a hydrodynamic and a contact contribution. Plotted together with the total stresses from (Gallier et al., 2014).

The particle stresses in the x, y and z directions are plotted together in Figure 7-20. From this it becomes clear that for the every case with $\phi \leq 0.5$ the relation $\sigma_{xx} > \sigma_{zz} > \sigma_{yy}$ holds. As a result the normal stress differences N_1 and N_2 are both negative for those cases. The particle layering in the core for the case of $\phi = 0.6$ results in significantly different relationships between the individual normal particle stresses.

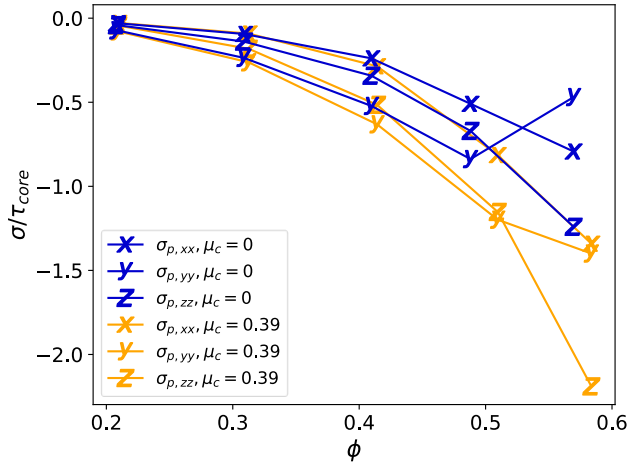

Figure 7-20, Normal particle stresses $\sigma_{p,xx}, \sigma_{p,yy}$ and $\sigma_{p,zz}$ normalised with τ_{core}, plotted together for the core regions of frictional and frictionless cases.

The normal stress differences can be determined with the normal particle stresses using equations (6.15) and (6.16). Figure 7-21 and Figure 7-22 give the results for N_1 and N_2 respectively as a function of ϕ. Corresponding numerical results from literature are also plotted (Gallier et al., 2014) (Seto & Giusteri, 2018). Besides that, a decomposition of the stress differences in a collisional and a hydrodynamic contribution is given for both normal stress differences. For N_1 a negative trend can be observed for the more dilute suspensions with $\phi \leq 0.4$, which is in agreement with results of (Gallier et al., 2014). The value of N_1 for the frictional case of $\phi = 0.5$ shows the start of a positive trend however, indicating that $\sigma_{p,yy}$ is getting less negative compared to $\sigma_{p,zz}$. This can be the result of particle layering in the core since we know from Figure 7-5 that this effect is present for the cases with $\phi \geq 0.5$. On the other hand this positive trend is also observed by (Seto & Giusteri, 2018) for $\phi > 0.4$ in the absence of particle layering, suggesting that this is a rheological effect in unbounded suspensions. This could especially be the case for the frictional case of $\phi = 0.5$, since the PDF for the core region of this suspension in Figure 7-7 shows no strong particle layering. From the decomposition of N_1 it is clear that this transition from a negative to a positive trend comes from the change in the hydrodynamic contribution. For the most dense cases the results deviate significantly from the results of (Seto & Giusteri, 2018), which is an effect of particle layering in the core. From this deviation it is clear that particle layering strongly promotes positive values of N_1 through the collisional contribution.

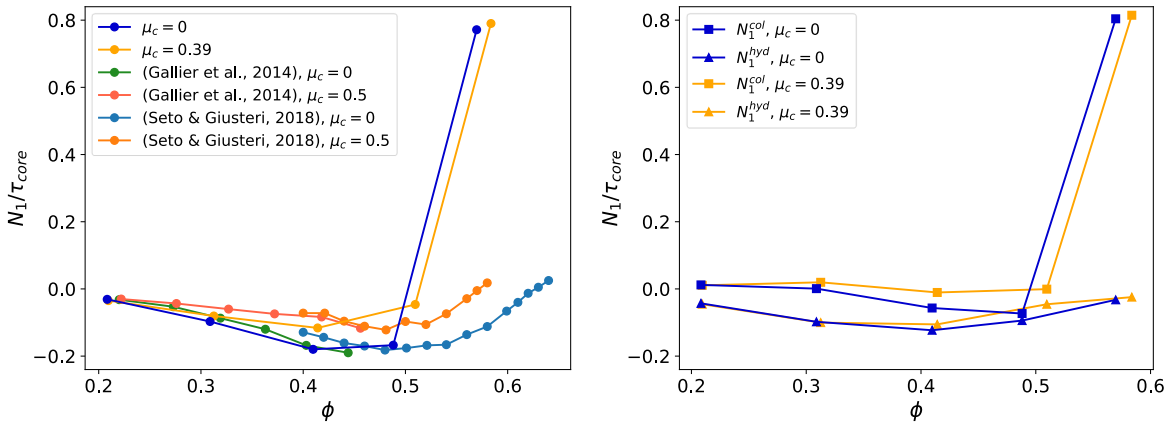

Figure 7-21, The normalised first normal stress difference N_1/τ_{core} plotted as a function of ϕ for the core regions of both the frictional and the frictionless cases. Plotted together with numerical results from literature (Gallier et al., 2014) (Seto & Giusteri, 2018). On the right a decomposition of the stress difference in a collisional (■) and a hydrodynamic contribution (▲) is given.

The second normal stress difference N_2 shows a negative trend only, and the friction factor seems to promote an even steeper negative trend. Similar results are found for the simulations of (Gallier et al., 2014). The datapoints for the frictionless case however do not fall exactly on the same line. From the contributions we can clearly see that the collisional contribution is dominant for N_2, the hydrodynamic contribution is significantly smaller and has a positive sign instead. For the most dense cases with $\phi = 0.6$ it is clear that particle layering in the core promotes an even more negative N_2 through the collisional contribution.

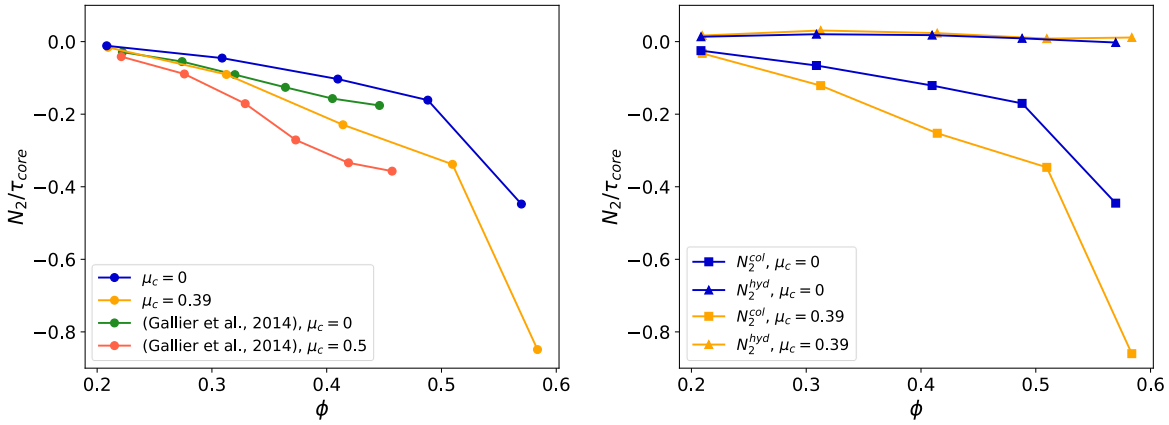

Figure 7-22, The normalised second normal stress difference N_2/τ_{core} plotted as a function of ϕ for the core regions of both the frictional and the frictionless cases. Plotted together with numerical results from literature (Gallier et al., 2014). On the right a decomposition of the stress difference in a collisional (■) and a hydrodynamic contribution (▲) is given.

7.5.2 Normal particle stresses in a confined suspension

Particle layering has a strong effect on normal particles stresses in the wall region. The time-averaged normal stress profiles for the frictionless and the frictional case with $\phi = 0.5$ are given in Figure 7-23. Normal stresses in this plot are normalized with the total shear stress $\tau_{tot} = \eta_{r,tot}/Re_{\dot{\gamma}}$. From this figure we can clearly see that the normal particle stresses behave different near the walls. The normal stresses in the x and y-direction get less negative near the walls while the normal stress in the z-direction gets more negative close to the walls. This is a result of the particles moving in layers such that collisions will occur mainly in the wall-normal direction. From the comparison between the frictionless and the frictional case we can see that this effect spreads further through the domain for lower friction factors.

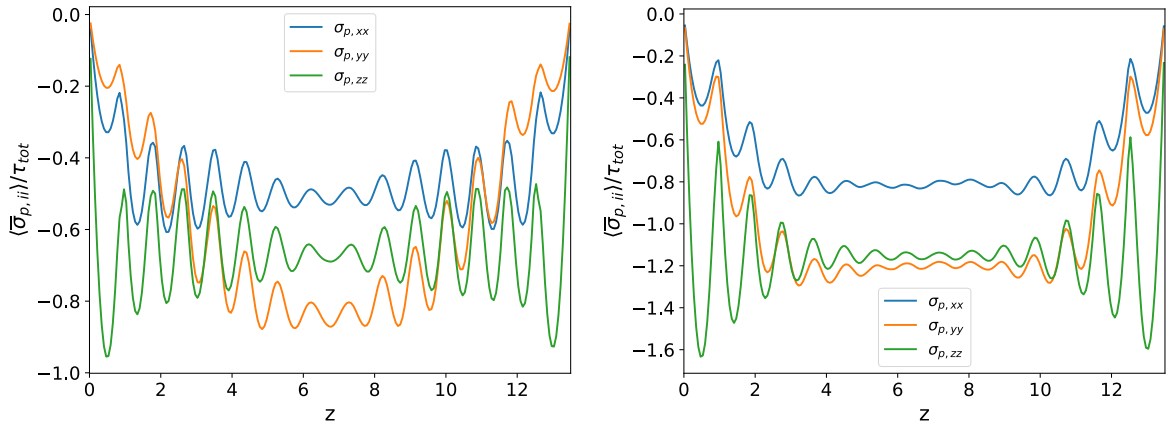

Figure 7-23, Time-averaged normal stress profiles for the frictionless (left) and the frictional (right) case $\phi = 0.5$.

As a result of the variations in the normal particle stresses, the normal stress differences will also vary in the wall regions. In Figure 7-24 the normal stress differences are plotted as a function of the wall-normal position z for the frictional case of $\phi = 0.5$. This figure also gives a decomposition of the normal stress differences in a hydrodynamic and a collisional contribution. From this result we can clearly see that the particle layering has a positive effect on N_1 and a negative effect on N_2, similar to the particle layering in the core region. Besides that, it is clear that the variations near the wall strongly originate from the collisional contributions to the normal particle stresses. The average values for N_1 and N_2 for the complete domain as a function of ϕ are given in Figure 7-25. In this figure the numerical results of (Gallier et al., 2016) are also plotted, which show a similar trend.

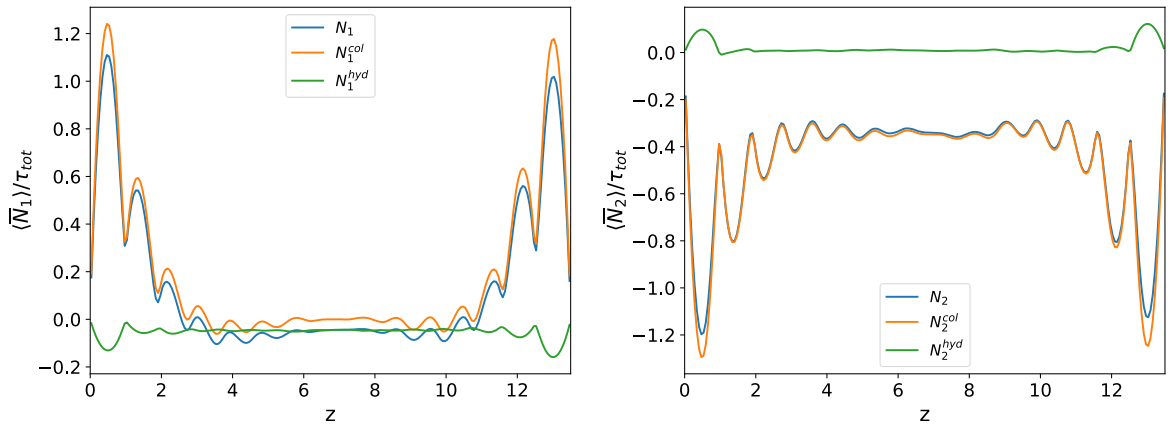

Figure 7-24, Time-averaged normal stress differences N_1 and N_2 for the frictional case of $\phi = 0.5$ as a function of wall-normal position. The collisional and hydrodynamic contributions to the normal stress differences are also given.

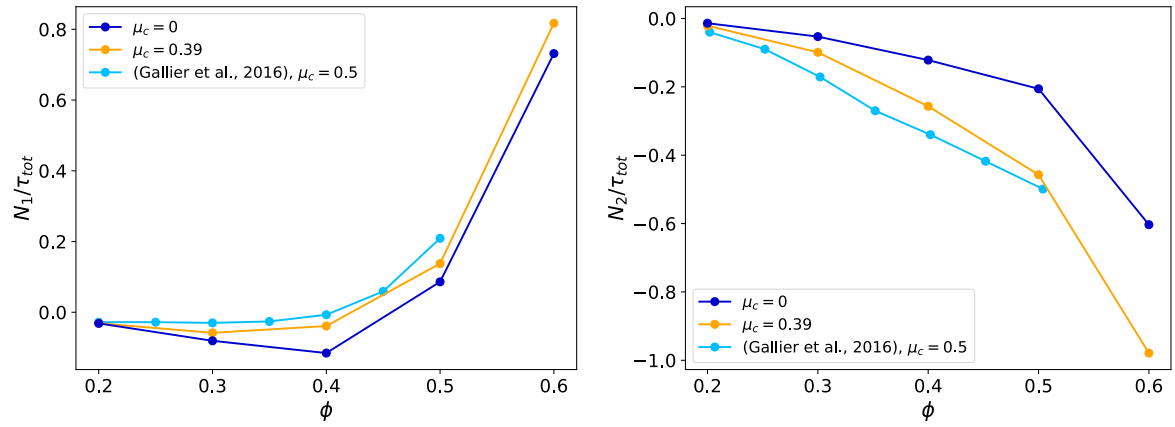

Figure 7-25, The first and second normal stress difference N_1 and N_2 for the whole domain as a function of ϕ. Plotted together with numerical results from literature (Gallier et al., 2016).

7.6 The effect of the coefficients of restitution

So far the normal and tangential coefficients of restitution were kept constant as $e_{n,d} = 0.97$ and $e_{t,d} = 0.1$. In this section the coefficients of restitution are varied to determine the effects on suspension rheology. Variations are made based around the frictional case of $\phi = 0.4$. For the normal coefficient this case was repeated with $e_{n,d} = 0.1$ and 0.5, and for the tangential coefficient with $e_{t,d} = 0.5$ and 1. So for both coefficients data points were obtained over the complete range between 0 and 1. In Figure 7-26 the normal particle stresses for the core region are plotted as a function of both $e_{n,d}$ and $e_{t,d}$. From these results it is clear that the normal particle stresses vary only slightly. Also for the particle shear stress $\sigma_{p,yz}$ only weak variations were found.

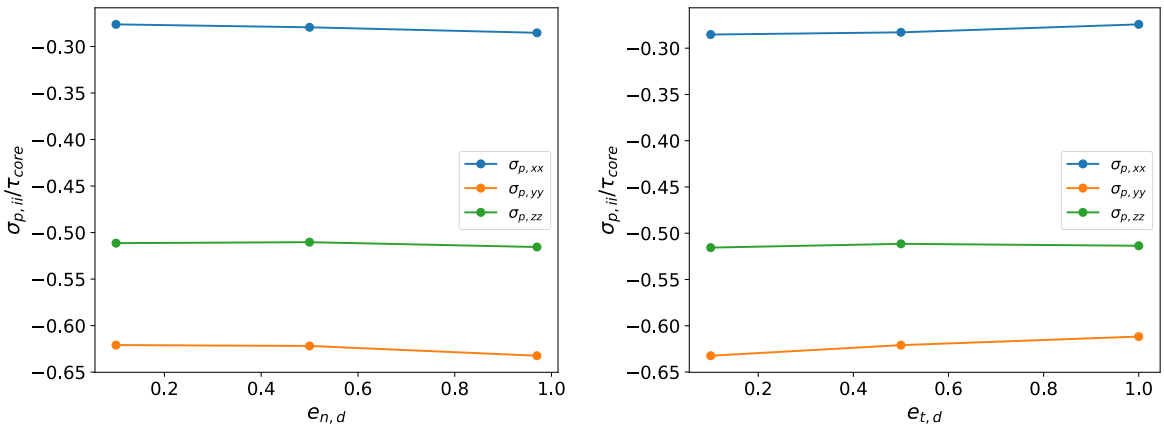

Figure 7-26, Normal particle stresses in the core region as a function of both normal coefficient of restitution $e_{n,d}$ (left) and the tangential coefficient of restitution $e_{t,d}$ (right). Variations of both coefficients are based on the frictional case of $\phi = 0.4$.

The weak variations of the particle stresses for varying coefficients of restitution can be explained by the fact particle interactions are overdamped by viscous forces. Particle inertia will be dominated by viscous forces, such that the loss of momentum due to a collision will have almost no effect. The coefficients of restitution can be more relevant for particle volume fractions closer to the jamming limit, as the contribution of particle contact to the particle stresses will grow with ϕ. Besides that, the coefficients of restitution might also be more relevant for higher Reynolds number flows, since particle inertia will play a larger role in that regime.

8 Conclusion and recommendations

In this work non-colloidal suspensions in Stokes flow were simulated using a second-order accurate Immersed Boundary Method (Breugem, 2012). Boundary conditions were defined in order to simulate a plane Couette flow between two flat walls. The goal of this work was to validate the capability of the IBM to simulate suspensions near the jamming limit. This is done by simulating various cases such that a comparison with existing numerical and experimental data can be made. The parameter space in this work exists of variations in the particle volume fraction ϕ and the coefficient of sliding friction μ_c.

All simulated cases show a wall-induced particle layering effect to some extent. The simulated domain was therefore separated in a core region and two wall regions for every case. This distinction made it possible to analyse the effect of particle layering separately from the un-layered rheology in the core, although the most dense cases show particle layering even in the core region. The microstructure of both regions was analysed using a pair distribution function (PDF). In general the PDFs agree well with existing numerical results (Gallier et al., 2014) (Yeo & Maxey, 2010a) and experimental results (Blanc et al., 2013). Slight differences were observed for the PDFs in the wall region compared to results from (Yeo & Maxey, 2010a), which may be caused by differences in the contact models used. The relative viscosity is determined for the core regions and for the complete domains. In the core regions the relative viscosity shows a similar trend compared to experimental results (Dbouk et al., 2013) (Zarraga et al., 2000), the relative viscosity is in general lower however. When the data is plotted as a function of ϕ/ϕ_m using a fit to the Marron & Pierce equation all results collapse on the same curve. In this work a maximum packing fraction of $\phi_m = 0.69$ is found for frictionless particles and $\phi_m = 0.635$ is found for a friction coefficient of $\mu_c = 0.39$. The results for the complete domain show that particle layering reduces the relative viscosity especially close to the jamming limit. The confined relative viscosity from the numerical work of (Gallier et al., 2016) shows a stronger decrease than found in this work, this can however be the result of the difference in channel height between both cases. Finally the normal particle stresses are analysed, with the main focus on the normal stress differences. The core regions without particle layering all show a negative N_1 and N_2, the most dense cases however show the start of a positive trend for N_1 as also observed by (Seto & Giusteri, 2018). Results for the complete domain show that particle layering promotes a positive N_1 and an even more negative N_2.

In general we can state that the IBM is able to reproduce existing numerical data. Some differences are found, but further research will be needed to make any conclusions about these differences. Furthermore this work contains results for simulations of suspensions closer to the jamming limit than known so far. Besides, the present results are obtained with an advanced soft-sphere collision model, including lubrication corrections for close approach of particles. This model has been extensively validated with collision experiments in a previous study. Comparison of the simulated data with experimental results shows more significant deviations. This can have multiple reasons for example the particles being polydisperse or non-spherical, which is likely the case to some extent in experimental set-ups. Experimental results also differ significantly from each other, this is best visible in the comparison of experimental results for N_1 (Figure 2-14). This suggests that there exist significant differences between these suspensions, which must be well defined in order to make a valuable comparison between results. Besides that, experimental research usually determines rheological properties by measuring stresses at the walls. From this work it is clear that stresses at the walls are not always representative for the stresses in the rest of the domain. Because of these uncertainties it is not yet possible to determine how accurately the IBM simulates dense suspension flows.

8.1 Recommendations

Various assumptions have been made in this work that may have an influence on how practical the results are. Therefore it is worth to test these assumptions in additional simulations. One of these assumptions is that the friction factors for particle-particle and particle-wall collisions are equal. In practice this it is unlikely to be the case, since confining walls typically consist of other materials than the suspended particles. It can therefore be useful to vary the particle-wall friction factor independently in order to observe the effect on particle layering. Another assumption is that all particles have the same diameter, which is not the case in many practical examples. Results from (Pednekar et al., 2018) obtained with a discrete element method show that suspension rheology changes significantly by introducing polydispersity, it would therefore be interesting to further investigate the effects of polydispersity using DNS. And finally the particles in the current work are assumed to be perfectly spherical, while in practice particles can have a wide variety of different shapes. Therefore it would also be interesting to research the effect of shape variations on the suspension rheology. Many shape variations are possible, some suggestion are to use ellipsoidal-formed or faceted particles.

For future work on this topic it could also be useful to analyse simulated data in terms of the $\mu(I_v)$ rheology as described in section 2.2.5. This alternative view on suspension rheology can give some extra insights on effects of friction and the consequences of particle layering. Besides that, it was difficult to determine the un-layered rheology of dense suspensions in the current work as particle layering was present in the complete domain for the most dense cases. Increasing the domain height would help, but this comes with a strong increase in computational costs and very close to the jamming limit a completely layered domain might be inevitable. Therefore it is recommended to take measures against particle layering in order to study unbounded suspension rheology. The use of bumpy-walls, modelled as sheets of particles, instead of flat walls turns out to prevent the formation of particle layering according to (Chun et al., 2017). This strategy might make it possible to study the unbounded rheology of dense suspensions with relatively low computational costs.

Bibliography

3DPRINTING.com. (2019). *Swedish Municipalities Look to 3D Printed Food For the Elderly*. Retrieved from 3Dprinting.com: https://3dprinting.com/news/swedish-3d-printed-food-elderly/

Bae, C.-J., & Halloran, J. (2019). Concentrated Suspension-based Additive Manufacturing – Viscosity, Packing density, and Segregation. *Journal of European Ceramic Society*, 39, 4299-4306.

Batchelor, G., & Green, J. (1972). *The determination of the bulk stress in a suspension of spherical particles to order c^2.* J. Fluid Mech. 56.

Beer Holthuis. (2018). *Paper Pulp Printer*. Retrieved from beerholthuis.com: http://www.beerholthuis.com/portfolio/paper-pulp-printer/

Blanc, F., Lemaire, E., Meunier, A., & Peters, F. (2013). Microstructure in sheared non-Brownian concentrated suspensions. *J. Rheology*, 57, 273-292.

Boyer, F., Guazaelli, E., & Pouliquen, O. (2011). Unifying Suspension and Grannular Rheology. *Physical Review Letters*, 107, 188301.

Brady, J., & Bossis, G. (1988). Stokesian Dynamics. *Ann. Rev. Fluid Mech.*, 20:111-57.

Breugem, W.-P. (2012). A second-order accurate immersed boundary method for fully resolved simulations of particle-laden flows. *Journal of Computational Physics*, 231, 4469-4498.

Chun, B., Kwon, I., Hyun, W., & Jea, C. (2017). Lattice Boltzmann simulation of shear-induced particle migration in plane Couette-Poiseuille flow: Local ordering of suspension. *Physics of Fluids 29*, 121605.

Costa, P., Westerweel, J., & Breugem, W.-P. (2015). *Collision model for fully-resolved simulations of flows laden with finite-size particles.* Delft: Delft University of Technology.

Dbouk, T., Lobry, L., & Lemaire, E. (2013). Normal stresses in concentrated non-Brownian suspensions. *J. Fluid Mech. 715*, 239-272.

Deen, N., Peters, E., Padding, J., & Kuipers, J. (2014). Review of direct numerical simulations of fluid-particle mass momentum and heat transfer in dense gas-solid flows. *Chemical Engineering Science*, 116, 710-724.

Eilers, H. (1941). Die viskosität von Emulsionen hochviskoser Stoffe als Funktion der Konzentration. *Kolloid-Zeitschrift 97*, 313-321.

Einstein, A. (1911). *Berichting zu meiner Arbeid: Eine neue Bestimmung der Moleküldimensionen.* Berlin: Ann. Phys.

Gallier, S., Lemaire, E., & Peters, F. (2014). *Rheology of sheared suspensions of rough frictional particles.* Journal of Fluid Mechanics: ResearchGate.

Gallier, S., Lemaire, E., Lobry, L., & Peters, F. (2016). Effect of confinement in wall-bounded non-colloidal suspensions. *J. Fluid Mech. 799*, 100-127.

Guazelli, E., & Pouliquen, O. (2018). Rheology of dense granular suspensions. *J. Fluid Mech.*, 852.

Haeri, S., & Shrimpton, J. (2012). On the application of immersed boundary, fictitious domain and body-conformal mesh methods to many particle multiphase flows. *International Journal of Multiphase Flow 40*, 40, 38-55.

Jana, S., Kapoor, B., & Acrivos, A. (1995). Apparent wall slip velocity coefficients in concentrated suspensions of noncolloidal particles. *J. Rheol. 39*, 1123-1132.

Joseph, G., & Hunt, M. (2004). Oblique particle-wall collisions in a liquid. *J. Fluid Mech, vol. 510*, 71-93.

Joseph, G., Zenit, R., Hunt, M., & Rosenwinkel, A. (2001). Particle-wall collisions in a viscous fluid. *Journal of Fluid Mechanics 433*, 329-346.

Krieger, I., & Dougherty, T. (1959). *PhD thesis.* Cleveland: Case Institute of Technology.

Lashgari, I., Picano, F., Breugem, W.-P., & Brandt, L. (2014). Laminar, Turbulent and Intertial Shear-Thickening Regimes in Channel Flow of Neutrally Buoyant Particle Suspensions. *Physical Review Letters*, 113, 254502.

Luo, K., Wang, Z., Fan, J., & Cen, K. (2007). Full-scale solutions to particle-laden flows: Multidirect forcing and immersed boundary method. *Physical Review E.*, 76, 066709.

Mari, R., Seto, R., & Morris, J. (2014). Shear thickening, frictionless and frictional rheologies in non-Brownian suspensions. *Journal of Rheology*, 58, 1693.

Maron, S., & Pierce, P. (1956). *J. Colloid Sci.*, 11,80.

Material District. (2020, November 25). *Turning waste concrete into 3D printed public furniture*. Retrieved from Materialdistrict.com: https://materialdistrict.com/article/turning-waste-concrete-into-3d-printed-public-furniture/

McCormack, A., Highley, C., Leslie, N., & Melchels, F. (2020). 3D Printing in Suspension Baths: Keeping the Promises of Bioprinting Afloat. *Trends in Biotechnology*, Vol. 38, No.6.

Mittal, R., & Iaccarino, G. (2005). Immersed boundary method. *Annu. Rev. Fluid Mechanics*, 37: 239-61.

Morris, J. (2009). A review of microstructure in concentrated suspensions and its implications for rheology and bulk flow. *Rheol Acta*, 48:909-923.

Morris, J. (2020). Toward a fluid mechanics of suspensions. *Physical Review Fluids*, 5, 110519.

Morris, J., Denn, M., & Bonn, D. (2018). Shear thickening in concentrated suspensions of smooth spheres in Newtonian suspending fluids. *Soft Matter*, 14, 170.

Pednekar, S., Chun, J., & Morris, J. (2018). Bidisperse and polydisperse suspension rheology at large solid fraction. *Journal of Rheology*, 62, 513.

Picano, F., Breugem, W.-P., Mitra, D., & Brandt, L. (2013). Shear Thickening in Non-Brownian Suspensions: An Excluded Volume Effect. *Physical Review Letters*, 111, 098302.

Ryohei Seto, R. M. (2013). *Discontinuous Shear Thickening of Frictional Hard-Sphere Suspensions.* New York: Viewpoint.

Schwentenwein, M., & Homa, J. (2014). Additive Manufacturing of Dense Alumina Ceramics. *Int. J. Appl. Technol.* , 1-7.

Seto, R., & Giusteri, G. (2018). Normal stress differences in dense suspensions. *J. Fluid Mech. 857*, 200-215.

Southeast Asia Construction. (2018). *Control flow concrete 'could help solve skills shortage in Asia'*. Retrieved from Tradelinkmedia.biz: https://www.tradelinkmedia.biz/publications/7/news/1350

Stickel, J., & Powell, R. (2005). Fluid Mechanics and Rheology of Dense Suspensins. *Annu. Rev. Fluid Mech*, 37:129-149.

Stone-Ideas. (2020, August 22). *Science: the role of trouts in sediment transport in rivers, rivers shifting their beds due to climate change, monitoring the eruptions of a Guadeloupe volcano, and cremation since 7000 BC*. Retrieved from Stone-ideas.com: https://www.stone-ideas.com/80192/science-about-our-planet/

Vecteezy. (2022). *Blood Flow Graphics.* Retrieved from Vecteezy.com: https://www.vecteezy.com/free-vector/blood-flow

Yeo, K., & Maxey, M. (2010a). Dynamics of concentrated suspensions of non-colloidal particles in Couette flow. *J. Fluid Mech. 649*, 205-231.

Yeo, K., & Maxey, M. (2010b). Ordering transition of non-Brownian suspensions in confined steady shear flow. *Physical Review E 81*, 051502.

Zarraga, I., Hill, D., & Leighton, D. (2000). The characterization of the total stress of concentrated suspensions of noncolloidal spheres in Newtonian fluids. *J. Rheol. 44*, 185.